chemosensors

MDPI

Review

Recent Progresses in NIR-II Luminescent Bio/Chemo Sensors Based on Lanthanide Nanocrystals

Tingyu Yang [1,2], Jinglei Qin [3], Jinling Zhang [1,2], Lanying Guo [4], Mu Yang [3], Xi Wu [2], Mei You [2] and Hongshang Peng [2,*]

[1] College of Life and Environmental Science, Minzu University of China, Beijing 100081, China; 20400265@muc.edu.cn (T.Y.); 21400280@muc.edu.cn (J.Z.)
[2] College of Science, Minzu University of China, Beijing 100081, China; 19301334@muc.edu.cn (X.W.); 19301332@muc.edu.cn (M.Y.)
[3] Key Laboratory of Luminescence and Optical Information, Ministry of Education, Institute of Optoelectronic Technology, Beijing Jiaotong University, Beijing 100044, China; 19118040@bjtu.edu.cn (J.Q.); 17118448@bjtu.edu.cn (M.Y.)
[4] School of Medical Imaging, Wannan Medical College, Wuhu 241002, China; 16118431@bjtu.edu.cn
* Correspondence: hshpeng@bjtu.edu.cn

Abstract: Fluorescent bio/chemosensors are widely used in the field of biological research and medical diagnosis, with the advantages of non-invasiveness, high sensitivity, and good selectivity. In particular, luminescent bio/chemosensors, based on lanthanide nanocrystals (LnNCs) with a second near-infrared (NIR-II) emission, have attracted much attention, owing to greater penetration depth, aside from the merits of narrow emission band, abundant emission lines, and long lifetimes. In this review, NIR-II LnNCs-based bio/chemo sensors are summarized from the perspectives of the mechanisms of NIR-II luminescence, synthesis method of LnNCs, strategy of luminescence enhancement, sensing mechanism, and targeted bio/chemo category. Finally, the problems that exist in present LnNCs-based bio/chemosensors are discussed, and the future development trend is prospected.

Keywords: lanthanide nanocrystals; NIR-II luminescence; core-shell; sensing mechanism; bio/chemo sensor

check for updates

Citation: Yang, T.; Qin, J.; Zhang, J.; Guo, L.; Yang, M.; Wu, X.; You, M.; Peng, H. Recent Progresses in NIR-II Luminescent Bio/Chemo Sensors Based on Lanthanide Nanocrystals. *Chemosensors* **2022**, *10*, 206. https://doi.org/10.3390/chemosensors10060206

Academic Editor: Camelia Bala

Received: 25 April 2022
Accepted: 23 May 2022
Published: 30 May 2022

1. Introduction

Bio/chemical detection is of great significance in biological research and medical diagnosis [1,2]. So far, various detection methods have been developed, such as colorimetry [3], chromatography [4], electrochemical method [5], and fluorescence spectroscopy [6]. These methods have the disadvantages of complicated operation processes, low sensitivity, inability to perform real-time detection, and in vivo application compared with fluorescent spectroscopy. Fluorescent spectroscopy is a new type detection method, which has the advantages of high sensitivity, good selectivity, low detection limit, and high resolution [7,8]. Meanwhile, it may be applied to real-time monitoring of biological substances [9].

Fluorescent spectroscopy is divided into visible, NIR-I (700~900 nm), and NIR-II (1000~1700 nm), according to the different emission wavelengths [10–13]. Nevertheless, the autofluorescence generated (Figure 1a) [14], interference of scattering (Figure 1b) [14], and absorption (Figure 1c) [15] in the biological tissues severely limits the application of visible light and NIR-I in the biological body when the excitation and emission light pass through biological tissues [14,15]. In this wavelength range, especially, the scattering and autofluorescence of organisms are significant, forming a strong signal background and interference. To circumvent these restrictions, NIR-II has been emerging in recent years since it can dramatically reduce scattering lights (Figure 1d) [16] and increase penetration depth (Figure 1e) [17–19] in biological applications, compared with those emitting in the

visible or the NIR-I. Therefore, the research on NIR-II luminescent materials has gradually increased in bioimaging and bio/chemical sensing due to the unique superiority of NIR-II luminescent materials (Figure 2).

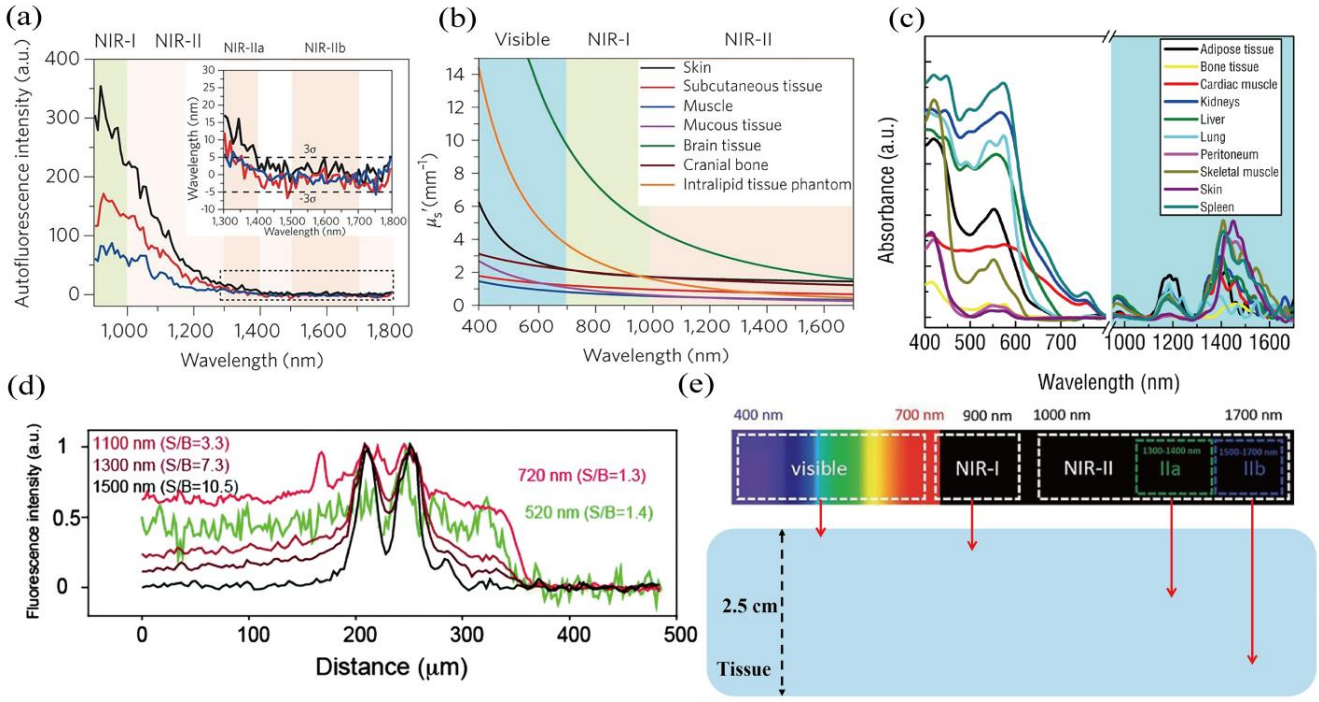

Figure 1. (**a**) Autofluorescence spectra of mouse liver (black), spleen (red), and heart tissue (blue) under 808 nm light. Inset shows the enlarged results at longer wavelengths. (**b**) Scattering coefficients of intralipid tissue phantoms and various biological tissues in the wavelength range of 400~1700 nm. (**a**,**b**) Adapted, with permission, from Ref. [14]. Copyright 2017, Springer Nature. (**c**) Absorbance spectra of various biological tissues. Adapted, with permission, from Ref. [15]. Copyright 2013, Springer Nature. (**d**) Line profile analysis of the fluorescence intensities in the lymph system of a mouse. The values of the S/B express signal to background ratios in the fluorescence intensities. Adapted, with permission, from Ref. [16]. Copyright 2014, Royal Society of Chemistry. (**e**) Schematic of the imaging depth in tissues for visible, NIR−I, and NIR−II light, respectively.

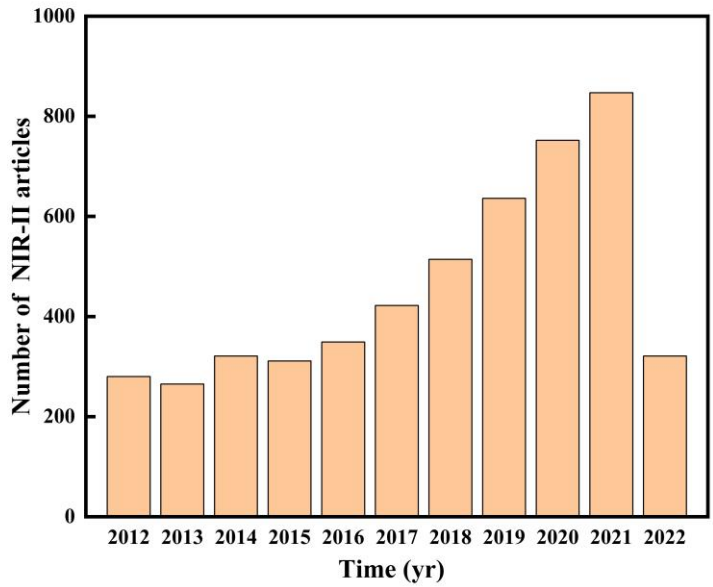

Figure 2. The number of published articles on NIR-II in the past ten years, based on Web of Science.

The current study of NIR-II luminescent materials mainly includes the following: quantum dots (QDs) [20,21], single carbon nanotubes (SWCNTs) [22], organic fluorescent probe [23–29], and lanthanide nanocrystals (LnNCs) [30–37]. Most QDs contain heavy metal elements such as lead, mercury, or arsenic [20]. This potential biological toxicity severely limits the application of QDs in organisms. The low luminescence quantum yield (<0.1%) and poor biocompatibility of SWCNTs limit their application in NIR-II [22]. Organic probes generally face extremely low fluorescence quantum yield, poor water solubility, and are prone to photobleaching and fluorescence quenching, which greatly limit the application of organic fluorescent probes in vivo [23–29]. Meanwhile, the emission wavelength of organic probes is short, most of which are around 1000 nm, which severely limits its application in the second near-infrared region [27,29]. In contrast, lanthanide ions (Ln^{3+}) have a unique 4f electronic structure [38–40]. The spectrum produced by the f-f transition has narrow-band emission characteristics and is not sensitive to the environment, and the emission only involves atomic transitions, so they have strong resistance to photobleaching [12,38–40]. Meanwhile, the Ln^{3+} can effectively protect the internal 4f orbitals from the interference of the external crystal field due to the $5s^2 5sp^6$ electron orbitals, make Ln^{3+} have a longer luminescence lifetime, and effectively avoid the interference of the autofluorescence of biological tissues [41,42]. Therefore, LnNCs, as a new generation of NIR-II probes, with low photobleaching, long luminescence lifetimes, low long-term cytotoxicity, narrow emission band widths, chemical stability, and large Stokes shifts, have gained more attention recently for bioimaging applications and bio/chemo sensors.

At present, the reviews on LnNCs mainly focus on discussing the application of LnNCs for in vivo imaging [12,38–42], and the discussion of LnNCs in bio/chemo sensing is only briefly mentioned as part of the imaging application. Therefore, a comprehensive and detailed review of NIR-II LnNCs in bio/chemo sensing is of great significance for researchers to thoroughly understand the research progress of LnNCs in bio/chemo sensing, and to provide ideas for the design of NIR-II LnNCs sensing probes. In this review, the latest research progress on NIR-II LnNCs bio/chemo sensors has been retrospected. Firstly, the design and synthesis of NIR-II LnNCs are discussed from a spectral point of view. Secondly, various application fields and sensing mechanisms of bio/chemo sensors are categorized and commented. Finally, the disadvantages of NIR-II LnNCs chemo/bio sensors and their prospects are given.

2. Design and Synthesis of NIR-II LnNCs

2.1. Mechanisms of NIR-II Luminescence

In LnNCs, three components are commonly included: a host matrix, a sensitizer, and an activator [36–42]. The host material should meet the requirements of optical transparency and low lattice phonon energy. At present, fluoride is mainly used as the host. The sensitizers and activators are generally Ln^{3+}. Nd^{3+}, Er^{3+}, and Yb^{3+} are demonstrated to be efficient sensitizers due to their large absorption cross-sections in NIR-I or NIR-II regions (Figure 3a) [36]. The absorption peaks of Nd^{3+} are located at 730 nm and 808 nm; the absorption peaks of Er^{3+} are located at 808 nm, 980 nm, and 1550 nm; the absorption peak of Yb^{3+} is located at 980 nm.

The activators with NIR-II emission mainly include Pr^{3+}, Nd^{3+}, Ho^{3+}, Er^{3+}, and Tm^{3+} (Figure 3a,b) [36,41]. To overcome the weak light absorption problem of the activator ion itself, sensitizers with higher absorption coefficients are co-doped into the host, serving to harvest the excitation photons and transfer the excitation energy to activators, thus populating the radiative transition of activators for NIR-II luminescence. Therefore, NIR-II luminescence is the mechanism of LnNCs: firstly, the excited states of the sensitizers and activators split into different energy levels, in a ladder-like manner, in the crystal field maintained by the host matrix. The ground state electrons of the sensitizer are excited to the excited state under the excitation light of the appropriate wavelength. Then, the energy is transferred to the activator, and the activator is excited to the excited state. Finally, the excited state electrons return to the ground state and emit NIR-II luminescence (Figure 3b).

According to NIR-II emission of different activators, it can be roughly divided into three types of NIR-II probes [36,41,43,44]: (1) Er^{3+} based NIR-II probes. NIR-II emission at intense 1525~1550 nm can be generated through $^4I_{13/2} \rightarrow {}^4I_{15/2}$ radiative transition. (2) Nd^{3+} based NIR-II probes. The radiative energy transitions of $^4F_{3/2} \rightarrow {}^4I_{11/2}$ and $^4F_{3/2} \rightarrow {}^4I_{13/2}$ in Nd^{3+} enable the generation of intense NIR-II luminescence, peaked at 1060 and 1330~1340 nm, respectively. (3) NIR-II probes of other ions. In a similar radiative transition, NIR-II emission can also be realized from Ho^{3+} at 1155 nm ($^5I_6 \rightarrow {}^5I_8$), Pr^{3+} at 1289 nm ($^1G_4 \rightarrow {}^3H_5$), and Tm^{3+} at 1475 nm ($^3H_4 \rightarrow {}^3F_4$).

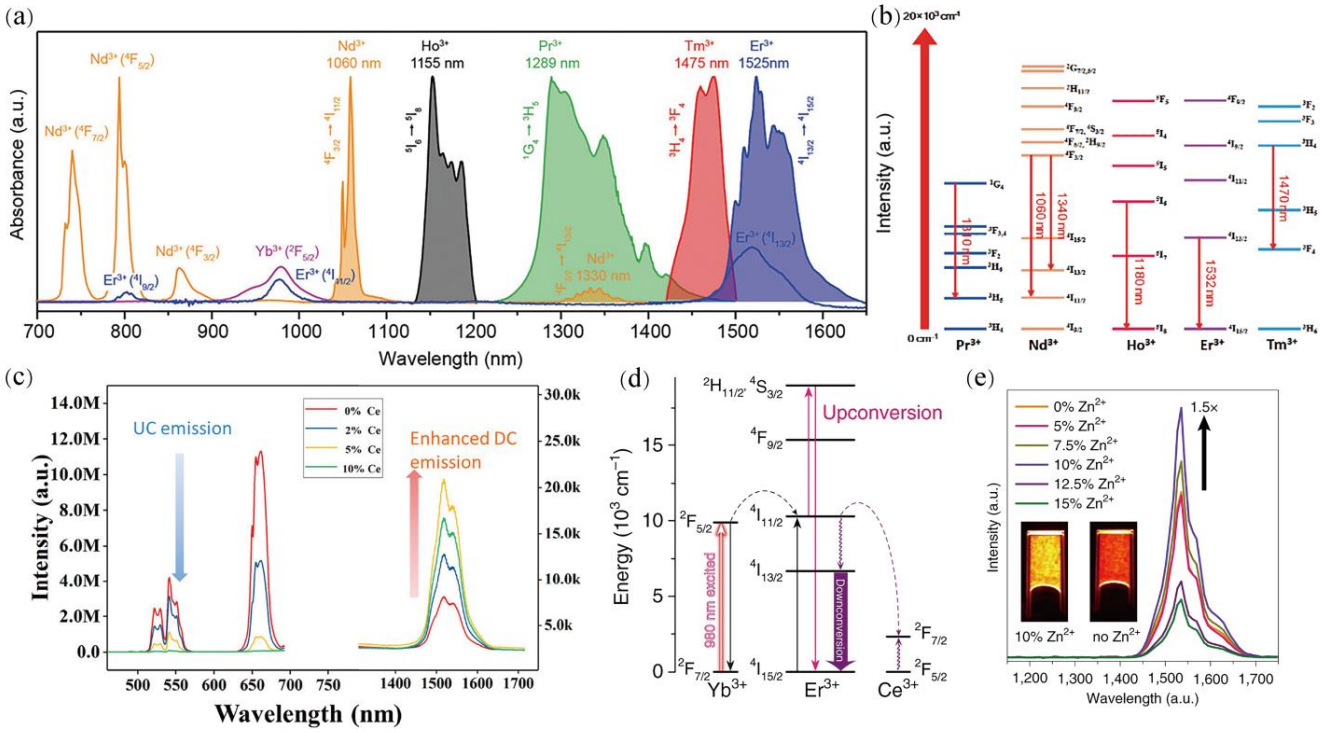

Figure 3. (**a**) Absorption (solid line) and NIR−II emission (solid line with color shade) spectra of different Ln^{3+}. Adapted, with permission, from Ref. [36]. Copyright 2019, Wiley−VCH. (**b**) Energy level diagram and energy transfer of Ln^{3+} with NIR−II characteristic emission. Adapted, with permission, from Ref. [41]. Copyright 2019, Springer Nature. (**c**) NIR-II spectra of LnNCs with different contents of Ce^{3+} concentrations. Adapted, with permission, from Ref. [45]. Copyright 2019, American Chemical Society. (**d**) The energy transfer between Yb^{3+}, Er^{3+}, and Ce^{3+}. Adapted, with permission, from Ref. [46]. Copyright 2017, Springer Nature. (**e**) NIR−II spectra of LnNCs with different Zn^{2+} concentrations. Adapted, with permission, from Ref. [47]. Copyright 2019, Springer Nature.

2.2. Strategies of Optimizing NIR-II Luminescence

The LnNCs with good luminescent efficiency can be obtained by rationally selecting the matrix, sensitizing ion, and activating ion. However, the luminescent efficiency of LnNCs is still low due to the inherent problems of LnNCs, which severely limits its application in sensing [38–42]. It is possible to design and optimize the structure of LnNCs to increase the quantum yield and enhance its luminescent intensity.

2.2.1. Ion Doping

It is possible to increase the luminescent intensity of a specific wavelength by adjusting the energy distribution of Ln^{3+}, in different luminescent bands, because of the multi-emission characteristics of Ln^{3+}. The up-conversion luminescence of LnNCs can be converted into down-conversion luminescence by doping other ions into LnNCs, and the NIR-II luminescence can be enhanced [45–47]. Li et al. [45] synthesized $NaLnF_4$: 40%Gd,

20%Yb, 2%Er, 5%Ce^{3+} nanorods (Ln = Y, Yb, Lu). The 1525 nm luminescence of Er^{3+} increased by 2.2 times, and the quantum efficiency reached 3.6% by doping Ce^{3+} to inhibit the up-conversion energy transfer of $NaLnF_4$ (Figure 3c). The incorporation of Ce^{3+} can promote the relaxation process of $^4I_{11/2}$ and $^4I_{13/2}$ of Er^{3+}, as well as shorten the life of the $^4I_{11/2}$ state, thereby inhibiting the up-conversion process and enhancing Er^{3+} luminescence at 1525 nm (Figure 3d) [46]. However, high Ce^{3+} concentration (10%) will also cause concentration quenching and reduce the luminescence of NIR-II (Figure 3c).

In addition, the luminescent intensity of LnNCs involves 4f-4f electronic transition forbidden effect [46,47]. This prohibition can be broken by doping with other ions, resulting in luminescent enhancement of LnNCs. Zhong et al. [47] designed and synthesized a Zn-doped α-$NaYbF_4$: 2%Er, 2%Ce, 10%Zn@$NaYF_4$ NIR-II luminescent probe. The doping of Zn weakened the 4f-4f electronic transition forbidden effect, resulting in enhancing the NIR-II luminescence. When the doping concentration of Zn was 10%, the luminescence of NIR-II was 1.5 times higher than that of undoped α-ErNPs (Figure 3e).

2.2.2. Core-Shell Structure

Due to the small size of LnNCs, the excited state energy of its luminescent ions is easily transferred to the surface of the nanocrystals, through inter-ion energy transfer, and quenched by various surface defects, ligands, or solvent molecules. Therefore, coating different shell layers on mononuclear LnNCs can inhibit its surface quenching and cross-relaxation, thereby enhancing NIR-II luminescence.

At present, the main thing is to wrap an inert shell on the surface of a single core [48–51]. However, it should be noted that the lattice matching, between the inert shell layer and the core, is the main factor to be considered in the preparation. If the lattice parameter gap is too large, it is difficult to form a complete core-shell coating structure. Therefore, considering the factors of lattice matching, common inert shell layers include $NaYF_4$, $NaLuF_4$, and CaF_2, etc. [49]. The luminescent intensity of the $NaYF_4$: 10%Yb^{3+}, 30%Nd^{3+}@CaF_2 core-shell structure at 1000 nm is 45 times higher than that of single-core $NaYF_4$: 10%Yb^{3+}, 30%Nd^{3+} under the excitation of 808 nm (Figure 4a) [48]. Likewise, Li et al. [49] completed a detailed investigation of the relationship between shell thickness and NIR-II emission intensity in the $NaErF_4$@$NaYF_4$ core/shell. As the inert shell path increases, the luminescence of Er^{3+} in NIR-II gradually increases (Figure 4b).

However, when the inert shell exceeds a certain thickness, it will weaken the light intensity received by the inner core, resulting in the weakening of the luminescent intensity. From Figure 4c, the luminescent intensity of LnNCs at 1525 nm was significantly reduced after $NaYF_4$: Yb^{3+}, Er^{3+} coated inert shell $NaLuF_4$ with a thickness of 13.2 nm [50]. Sun et al. [51] reported a highly efficient NIR-II luminescent $NaErF_4$@$NaYF_4$@$NaYF_4$: 10%Nd@$NaYF_4$ nanocrystal. The strong NIR-II luminescence was successfully obtained by adjusting the thickness of the $NaYF_4$ buffer layer, to limit the energy transfer between Er^{3+} and Nd^{3+}, and optimizing the thickness of the outermost $NaYF_4$ to passivate surface defects. Therefore, reasonable adjustment of the coating thickness of the inert shell layer and the position of the inert shell side can achieve high-efficiency luminescence in NIR-II.

In addition to wrapping the inert shell to achieve the enhancement of NIR-II luminescence, it can also wrap the active shell to enhance the NIR-II luminescence. The active shell layer refers to the presence of an activator or sensitizer in the shell layer, which mediates energy transfer and enhances the luminescence in the NIR-II [52]. Wang et al. [52] prepared β-$NaGdF_4$@Na (Gd, Yb) F_4: Er@$NaYF_4$: Yb@$NaNdF_4$: Yb. The Nd^{3+} in the outermost layer can be excited by an 800 nm laser, and the energy was transferred to Er^{3+} in the inner layer through Yb^{3+}, resulting in an enhancement of its 1525 nm luminescence emission. Its 1525 nm luminescence penetrates the pork tissue to a depth of 18 mm.

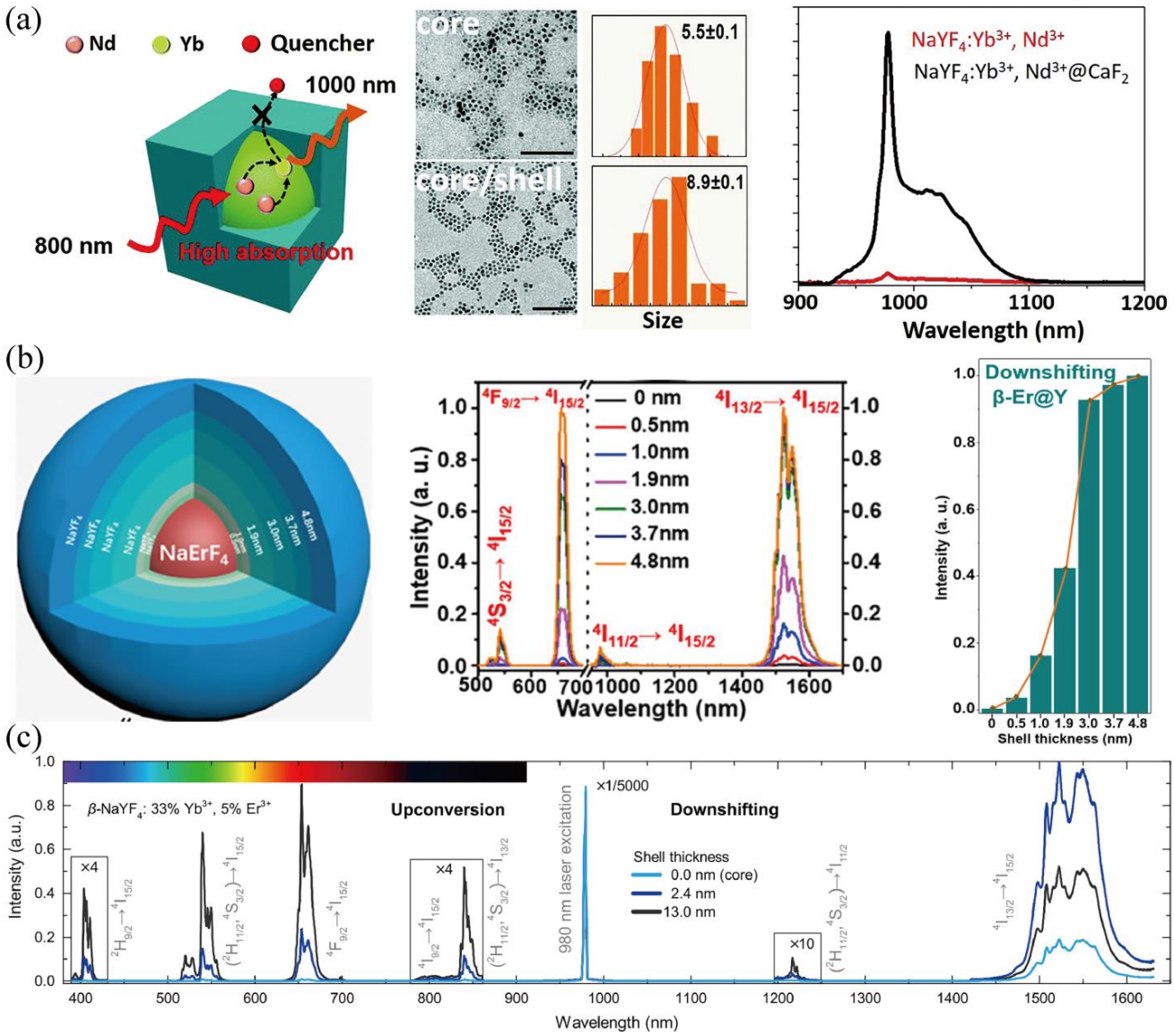

Figure 4. (**a**) Schematic illustration, TEM image and emission spectra of the core and core@shell. Adapted, with permission, from Ref. [48]. Copyright 2018, Royal Society of Chemistry. (**b**) Schematic illustration, NIR−II spectra and intensity of β-NaErF$_4$@NaYF$_4$. Adapted, with permission, from Ref. [49]. Copyright 2020, American Chemical Society. (**c**) NIR−II luminescence of NaYF$_4$: Yb^{3+}, Er^{3+} in different shell paths. Adapted, with permission, from Ref. [50]. Copyright 2016, American Chemical Society.

2.2.3. Dye-Sensitized Luminescence

The absorption coefficient of Ln^{3+}, in some specific wavelength bands, is very low, which greatly affects its luminescent intensity. The absorption coefficient of π-π transitions of some organic dyes is very high, has strong absorption in the spectrum 700~860 nm, and it can be used as a ligand to bind with Ln^{3+} [53–56]. The excited state energy level of the organic dye matches the excited state energy level of the Ln^{3+}, which can produce the energy transfer process, so that the LnNCs can carry out efficient NIR-II luminescence emission (Figure 5a) [54].

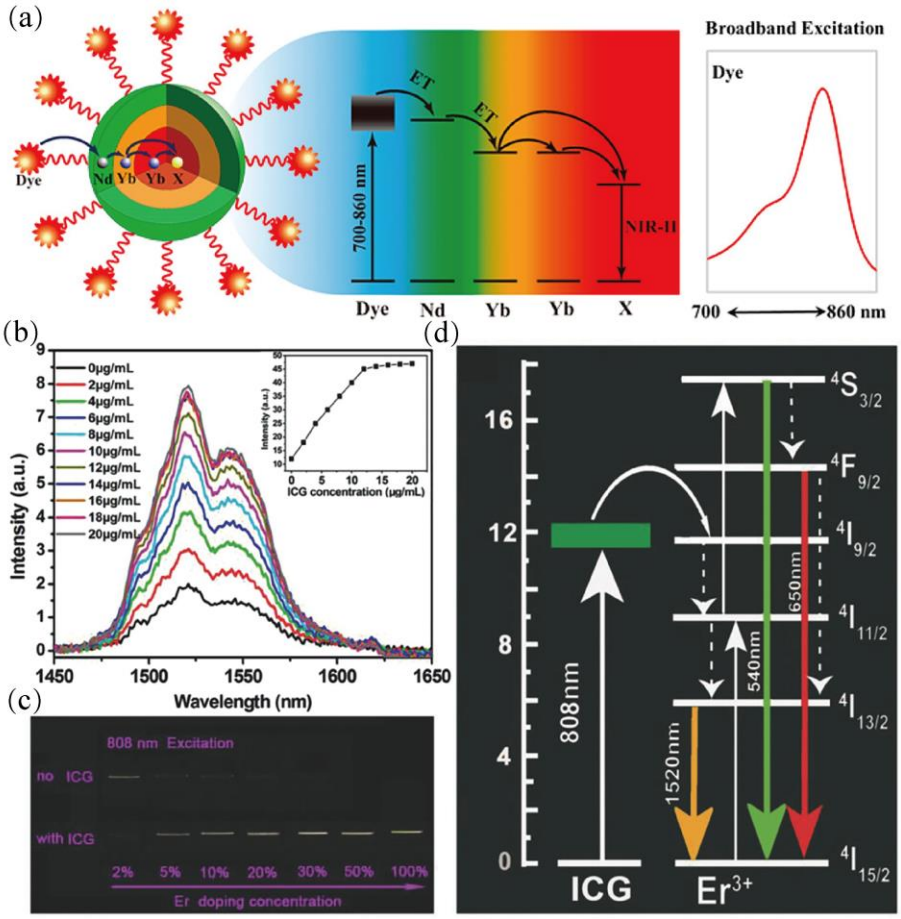

Figure 5. (**a**) Schematic illustrations of the energy transfer pathway from dye on the surface of LnNCs. Adapted, with permission, from Ref. [54]. Copyright 2016, American Chemical Society. (**b**) NIR−II fluorescence emission of LnNCs with different concentrations of ICG. (**c**) The luminescence photographs of LnNCs with ICG. (**d**) The mechanism of ICG-sensitized LnNCs. (**b**–**d**) Adapted, with permission, from Ref. [55]. Copyright 2018, Wiley−VCH.

Wang et al. [55] used indocyanine green dye (ICG) as an organic sensitizer to transfer energy to $NaYF_4$: Er nanoparticles to enhance the NIR-II luminescence (Figure 5b,c). ICG, as a donor with high absorption cross-section at 808 nm, increased the excitation efficiency of Er^{3+} through the energy transfer mechanism (Figure 5d). However, the NIR-II luminescent intensity decreased when the concentration of ICG was higher, which was ascribed to the self-quenching effect between the ICG (Figure 5b). The luminescence at 1525 nm was enhanced by 10 times at the optimal ICG concentration. Similarly, Ren et al. [56] modified LnNCs with dye-brush polymer (Dye-BP), which led to an impressive 675 times enhancement of NIR-II luminescence in aqueous solution. When the concentration of Dye-BP exceeds a certain concentration, it will also reduce the luminescence of NIR-II. Therefore, it is the key to choosing suitable organic dyes as sensitizers, but it is necessary to find the optimal concentration of organic dyes in the regulation of enhancing NIR-II luminescence to achieve the strongest NIR-II luminescence.

In addition to organic sensitizers, inorganic nanoparticles are also used as sensitizers to enhance the NIR-II luminescence of LnNCs due to their wide absorption and narrow emission and excellent resistance to photobleaching. Zhang et al. [57] introduced an inorganic nanoparticle sensitized system, which uses near-infrared-emitting Ag_2S QDs, as a sensitizer with broadband photon absorption, to enhance NIR-II luminescence. The NIR-II luminescence of LnNCs@Ag_2S enhanced ~17-fold in intensity and ~10-fold in

brightness over bare LnNCs because of increased absorptivity and overall broadening of the LnNCs@Ag_2S absorption spectrum.

Except for the main methods mentioned above, it is also possible to enhance NIR-II luminescence by controlling the size and crystal form of synthetic LnNCs [47]. However, due to the inherent properties of LnNCs and the complexity of the external environment (-OH) during application, it will severely quench the luminescence in the NIR-II. Therefore, enhancing the NIR-II luminescence is a difficult point in research.

2.3. Preparation Methods

The grain size, crystal phase, morphology and shell of LnNCs are all key parameters that directly affect their luminescence performance. Researchers have been committed to developing various methods to synthesize LnNCs with different properties, such as thermal decomposition, hydrothermal synthesis, co-precipitation, and sol-gel process [42]. The most commonly used methods are thermal decomposition [58–65], hydrothermal synthesis [66–71] and co-precipitation [72–81].

2.3.1. Thermal Decomposition

Thermal decomposition is the most popular method to synthesize high-quality monodisperse LnNCs [58–65]. Thermal decomposition is a synthesis process in which organic precursors of metal ions are dissolved in a high-boiling organic solvent and then decomposed at high temperatures to obtain corresponding metal fluoride products.

The LnNCs with different crystal phases and sizes can be synthesized by controlling different reaction parameters. Suter et al. [59] studied the crystal phase process of synthesizing $NaYF_4$ in oleic acid (OA) and octadecene by thermal decomposition method. There were three stages in this thermal decomposition synthesis process. The first stage was the nucleation and growth of small α-$NaYF_4$ (<300 °C); the next stage was the growth of α-$NaYF_4$ (300 °C, 60 min); the third stage was the phase transition from small α-$NaYF_4$ to larger β-$NaYF_4$ (300~310 °C, 30 min). Li et al. [60] also proved that α-$NaYF_4$ can be synthesized at low temperature, while β-$NaYF_4$ can be synthesized at high temperature, and the longer the time, the higher the crystallinity and the larger the particles. The content of OA in the reaction mainly affects the aspect ratio of the particles, and a high ratio of OA can synthesize a rod-like structure [60]. NH_4F provides F^- ions in the process, which affects the nucleation rate of LnNCs, thus affecting the size of LnNCs, and the high NH_4F content leads to the formation of small particles [58,60].

The LnNCs with different crystal types, sizes, and core-shell structures can be prepared using this method, especially for synthesizing ultra-small LnNCs. However, the requirements for the operation during the reaction and the amount of reactants added are particularly high when synthesizing small-sized materials, especially when the whole reaction is in an inert atmosphere. If oxygen enters, the OA oxidation solution will turn black and cause the reaction to fail. Wang et al. [58] studied, in detail, the problems and solutions that easily occur in synthesizing LnNCs via thermal decomposition. This has important guiding significance for the efficient synthesis of LnNCs.

2.3.2. Hydrothermal Synthesis

The hydrothermal synthesis usually occurs in a closed environment under high temperature and pressure. The high solubility and reactivity of the reactants in the sealed reaction vessel, under high temperature and high pressure, are used to grow nanocrystals in aqueous solutions (such as water or organic solvents) [42,66–71]. The reaction temperature is relatively low (generally less than 200 °C). It has become a simple and effective method to synthesize monodisperse LnNCs with adjustable morphology and structure [67,69,71].

Wang et al. [67] studied the effects of reactant concentration, temperature, and time on LnNCs. High concentration (Ln^{3+}) would result in nanorods, while low concentration resulted in nanoparticles. Higher temperature will decrease the length-to-diameter ratio of the as-prepared nanorods. Too short of a reaction time resulted in only nanoparticles instead

of nanorods. The morphology and size of LnNCs can also be controlled by controlling the amount of F^-. Qu et al. [69] used NH_4F as the F^- source to prepare $NaYF_4$ samples and found that different F^-/Y^{3+} ratios have a significant impact on the morphology, crystal phase, and size of the nanocrystals. The high molar ratio of F^-/Y^{3+} would benefit the α to β phase transition and formation of hexagonal phase products. The influence of different pH on the synthesis of LnNCs was also studied, $NaYF_4$ presented an octahedral morphology and a smooth surface (pH 1.5). When the pH was 6, $NaYF_4$ microtubules were formed [66].

The hydrothermal method can control the synthesis of LnNCs of different types of morphology, size, and crystal form, but the reaction rate of the system is slow, and it generally takes 20 h of reaction time to obtain monodisperse LnNCs with uniform size and morphology. The size is generally larger (sub-micron level). Meanwhile, it is difficult to observe the growth process of LnNCs. In addition, the operability of the hydrothermal reaction is slightly poor, so it is difficult to effectively control the growth of the core-shell structure.

2.3.3. Co-Precipitation

The co-precipitation method refers to the preparation of LnNCs with uniform composition in a variety of cationic solutions through a precipitation reaction after adding a precipitant [72–81]. Generally, the growth of LnNCs is controlled by adding ligands, such as polyvinylpyridinone (PVP), polyethyleneimine (PEI), or ethylenediaminetetraacetic acid (EDTA), to the solvent.

The co-precipitation method may be one of the most effective methods to prepare ultra-small LnNCs, and the size of LnNCs prepared by this method is uniform and controllable. Compared with other methods, this method does not need expensive equipment, the reaction conditions are relatively mild, the experimental operation process is relatively simple, and it saves time [75,78–81]. Yi et al. [78] improved this method and used simple water-soluble inorganic compounds as precursors to synthesize LaF_3 nanocrystals, with uniform size distribution and size around 5 nm. Guan et al. [79] employed a facile co-precipitation method to synthesize the pure hexagonal $NaYF_4$ and $NaYF_4$: Yb, Er by controlling the molar ratio of anions to cations at room temperature and ambient pressure. They can realize the crystal phase transition of LnNCs by controlling the pH of the precursor liquid and obtaining the hexagonal phase in the pH range of 5.0~6.5. The whole process does not use any organic additives, nor high temperature and high pressure, and it is an environmentally friendly technology suitable for large-scale industrial production.

However, the morphology of LnNCs, obtained by the co-precipitation method, is relatively simple, the surface is rough, and the morphology is difficult to control. In addition, the luminescence of LnNCs is also relatively weak, and annealing is generally required to improve the crystallinity of the material and to improve the luminescent intensity. After the annealing treatment, the surfactant wrapped on the surface of the LnNCs will be carbonized, which will destroy the hydrophilicity of the LnNCs and affect its subsequent application.

3. Sensing Mechanisms of NIR-II LnNCs

The energy gap between some Stark sublevels of Ln^{3+} is very small, and the thermal coupling is very strong. Small temperature variations may result in remarkable changes in their emitting intensity [41,82–84], which are thus used for temperature sensing. Recently, Nexha et al. [85] gave a comprehensive review on LnNCs-based temperature sensing.

Aside from temperature, LnNCs have no direct relationship with any physiological and biochemical characteristics, due to their relatively stable structure and spectral characteristics. Therefore, in the construction of LnNCs-based bio/chemo sensors, LnNCs work either as energy donors or reference units, which further combine with an appropriate responsive unit to specifically respond to a target of interest. Some inorganic ions and organic dyes were used as the responsive units [44,51,86–103], and typical LnNCs-based bio/chemo sensors are summarized in Table 1.

Table 1. Typical NIR-II LnNCs-based Bio/chemo sensors.

NIR-II LnNCs	Excitation (nm)	Emission (nm)	Response Unit	Influence Signal	Applications	Ref.
$NaCeF_4$: Er, Yb	980	1530	$Ce^{3+} \rightarrow Ce^{4+}$	1530	H_2O_2	[86]
$NaErF_4$: 2%Ho@$NaYF_4$	1530	980/1180	IR1061	980	H_2O_2	[44]
$NaErF_4$@$NaLuF_4$	980	654/1550	Cypate	654	·OH	[88]
$NaYF_4$: 18%Yb^{3+}, 2%Er^{3+}	808/980	1550	IR786s	808/1550	ROS	[89]
$NaYF_4$: 20% Yb and 2%Er@$NaYF_4$	808/980	1550	IR786s	808/1550	ROS	[90]
$NaYF_4$: 50%Er@$NaYF_4$	808/980	1550	Cy7.5	808/1550	HOCl	[91]
$NaYbF_4$: 5%Er, 5%Ce@$NaYF_4$: 20%Nd	808/980	1550	IR-783	808/1550	HOCl and ·OH	[92]
$NaYbF_4$: Er@$NaYF_4$: Yb@$NaYF_4$: Nd	808	925/1525	Cy925	925	HOCl	[93]
$NaYF_4$: 18%Yb^{3+}, 2%Er^{3+}	980	1150/1550	SeTT	1150	HOCl	[94]
$NaErF_4$@$NaYF_4$	808/980	1525	IR808	808/1525	HOCl	[95]
NaYF4: 20%Yb, 2%Er@NaYF4: 30%Nd	808/980	1550	4-nitrophenol-Cy7	808/1550	GSH	[96]
$NaYF_4$: 20%Yb, 2%Er@$NaYF_4$: 30%Nd	808	1530	HC-Ni	1530	GSH	[97]
$NaYF_4$@$NaYF_4$: 1%Nd^{3+}	808	1064	MY-1057	1060	$ONOO^-$	[98]
$NaErF_4$@$NaYF_4$@$NaYF_4$: 10%Nd@$NaYF_4$	808	1060/1525	A1094	1060	$ONOO^-$	[51]
$NaGdF_4$: 3%Nd@$NaGdF_4$	808	1060	Compound 1	1060	$ONOO^-$	[99]
$NaYF_4$: 20%Yb, 2%Er@$NaYF_4$	808/980	1050/1550	$Ag^+ \rightarrow Ag_2S$	808/1050	H_2S	[87]
$NaGdF_4$: 2%Nd@$NaGdF_4$	808	1060	Compound 1	1060	H_2S	[100]
$NaYF_4$: Gd, Yb, Er@$NaYF_4$: Yb	808/980	1053/1525	$Ag \rightarrow Ag_2S$	808/1053	H_2S	[101]
$NaGdF_4$: 5%Nd@$NaGdF_4$	730/808	1064	BSA-NPTAT	730/1064	BSA drug-release monitoring	[102]
$NaGdF_4$:Nd@$NaGdF_4$	808	1058	TA-Fe^{3+}	1058	PPi	[103]

3.1. Inorganic-Ion-Based Recognition Mechanism

The LnNCs are internally doped or connected to inorganic ions on the surface, that are responsive to the external environment, to increase and decrease the luminescence of the NIR-II, thereby constructing a probe with a specific response ability to the external environment (Figure 6a). Inorganic ions must first participate in the energy transfer process of LnNCs NIR-II luminescence, and the increase and decrease in NIR-II luminescence can be controlled by the change of ion valence. Secondly, inorganic ions must respond to the external environment, and the change of the external environment will affect the change of the valence state of ions, as to realize the sensing function.

Lei et al. [86] designed and synthesized an H_2O_2 activated $NaCeF_4$: Er, Yb NIR-II luminescent probe and realized the detection of uric acid (Figure 7a). Among them, the doped Ce^{3+} effectively enhanced the cross-relaxation process of $^2F_{7/2}$ (Ce^{3+}) + $^4I_{11/2}$ (Er^{3+}) $\rightarrow$ $^2F_{5/2}$ (Ce^{3+}) + $^4I_{13/2}$ (Er^{3+}) and greatly increased the number of excited state electrons of $^4I_{13/2}$ (Er^{3+}), thereby effectively inhibiting the up-conversion process and enhancing the down-conversion process, resulting in the nine-fold enhancement of the down conversion luminescence at 1530 nm. In this probe, Ce^{3+} existed as an external environmental responsive ion, which was used to construct a biosensing probe. Under the oxidation of H_2O_2, Ce^{3+} was oxidized to Ce^{4+}, which weakened the cross-relaxation process and caused the luminescence quenching of the 1530 nm emission (Figure 7b). This responsive probe could be used to detect H_2O_2 or biomolecules that can generate H_2O_2. For example, the detection limit of uric acid could be reduced to 25.6 nmol·L^{-1} by detecting H_2O_2 produced by the reaction of uric acid and uricase (Figure 7c), and its tissue depth could reach 10 mm in small animal imaging. Similarly, Wang et al. [87] realized the response to H_2S by attaching human serum albumin (HSA)-Ag^+ (HSA-Ag^+) to the surface of $NaYF_4$: 20%Yb, 2%Er@$NaYF_4$ (Figure 7d). In the presence of H_2S, Ag_2S QDs were formed in coated HSA through an H_2S-induced chemical reaction between H_2S and Ag^+, which emitted luminescence at approximately 1050 nm ($I_{808\ Ex/1050}$) on irradiation with an

808 nm (Figure 7e). However, the luminescence signal of the probe was stable at 1550 nm ($I_{980\ Ex/1550}$) under 980 nm excitation (Figure 7f), generating a H_2S concentration-dependent ratiometric $I_{1050/1550}$ signal. Using this probe, the endogenous H_2S could be real-time monitored, in vivo, by the ratio variation of luminescence signals in two channels of 1050 and 1550 nm.

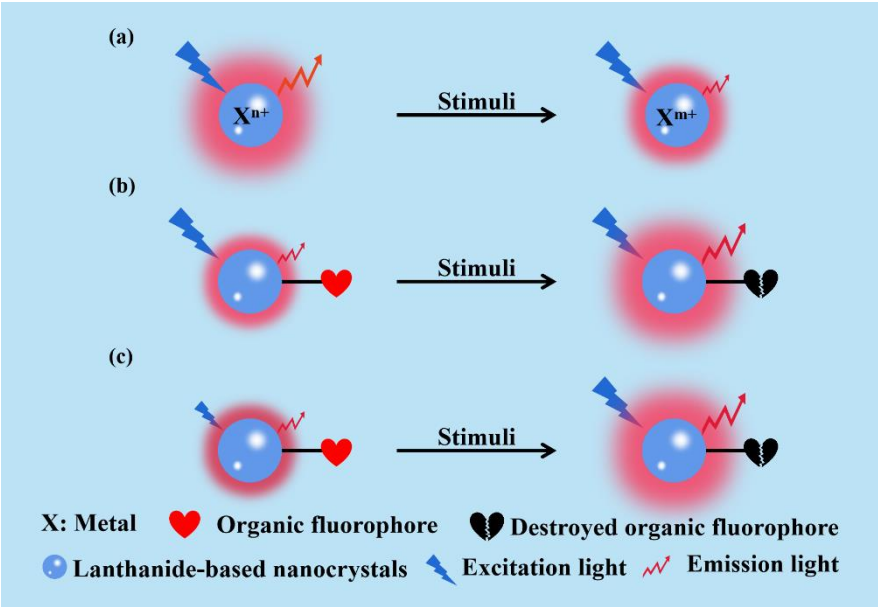

Figure 6. (**a**) Schematic illustration of an inorganic ion of LnNCs sensing. (**b**) Schematic of organic dyes on the surface of LnNCs for sensing by affecting the luminescence of LnNCs themselves. (**c**) Schematic of sensing that the surface organic dyes of LnNCs indirectly affect the luminescence by influencing the excitation light source.

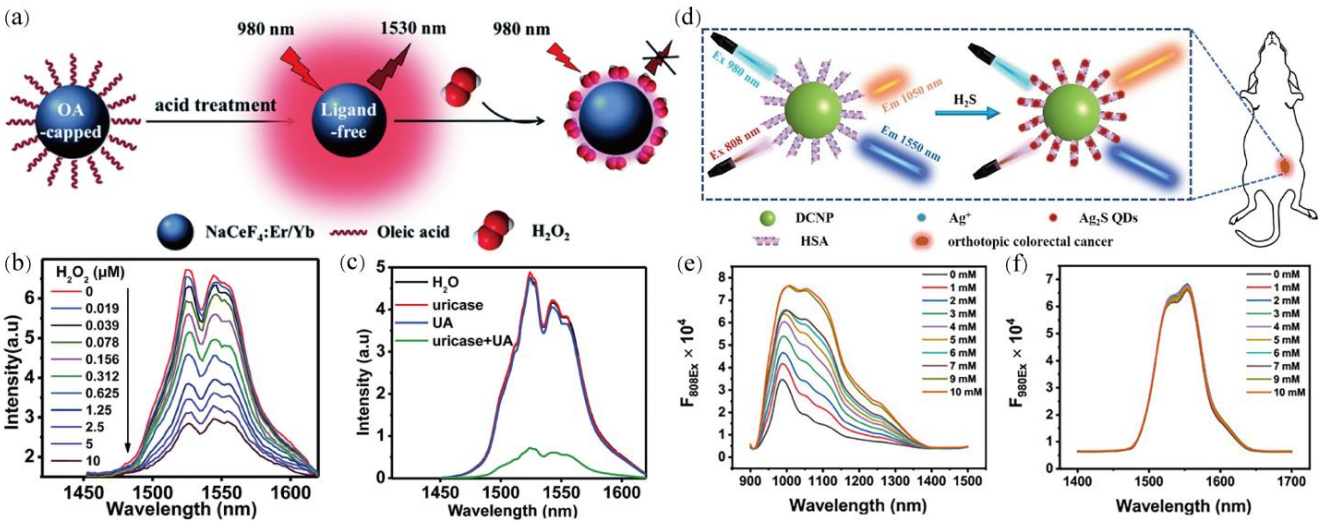

Figure 7. (**a**) Schematic of in sensing with $NaCeF_4$: Er, Yb nanoprobes. (**b**) NIR−II spectra of $NaCeF_4$: Er, Yb with different H_2O_2 concentrations. (**c**) NIR−II spectra of $NaCeF_4$: Er, Yb after the addition of H_2O, uricase, UA, and uricase + UA, respectively. Adapted, with permission, from Ref. [86]. Copyright 2018, Royal Society of Chemistry. (**d**) Schematic diagram of the endogenous H_2S−triggered in situ formation of Ag_2S in the LnNCs@HSA−Ag^+ nanoprobe for the NIR−II. (**e**,**f**) NIR−II spectra of the nanoprobe under 808 nm and 980 nm, respectively. Adapted, with permission, from Ref. [87]. Copyright 2021, American Chemical Society.

3.2. Organic-Dye-Based Recognition Mechanism

The LnNCs are hardly individually used for bio/chemo sensing, due to their non-responsive property. However, detection pathways involving chemical reactions are the most common methods due to their high selectivity and sensitivity. To realize the NIR-II sensing of LnNCs, organic dyes can be introduced to the surface of the LnNCs nanoparticles.

The LnNCs themselves do not have the ability to respond to the external environment, and the ability to respond to the external environment is mainly accomplished by organic dyes. Organic dyes must affect the luminescence of LnNCs to change the responsive signal. On the one hand, they directly act on the luminescence of LnNCs to affect the luminescence of LnNCs. That is, organic dyes and LnNCs undergo energy transfer or luminous absorption (Figure 6b). On the other hand, organic dyes affect the luminescence of LnNCs by affecting the intensity of the excitation light source (Figure 6c).

4. Category of Sensing

4.1. Biomedical Related Species

The pathological microenvironment of diseased tissues is obviously different from the physiological environment of normal tissues, such as abnormal redox environment (ROS, HClO, $ONOO^-$, GSH, and H_2S, etc.) [44,51,88–101]. These pathological parameters are exactly various diseases (such as cancer, inflammation, and cardiovascular disease) and essential biomarkers. According to the different response environments of LnNCs NIR-II probes, we have classified them.

4.1.1. Reactive Oxygen Species (ROS)

ROS including ·OH and H_2O_2, are widely present in organisms. It plays a vital role in physiological functions, which can regulate proteins, produce hormones, regulate cell signals, mediate inflammation, and eliminate pathogens [44,86,88–90].

Jia et al. [88] designed a cypate-modified $NaErF_4$@$NaLuF_4$ nanoprobe for detecting ·OH, on the basis of a typical reaction between cypate and·OH. Due to the presence of Er^{3+}, $NaErF_4$@$NaLuF_4$ could produce 1550 nm NIR-II luminescence and 654 nm luminescence under excitation at 980 nm. The cypate strongly absorbed the luminescence at 654 nm, resulting in luminescence quenching at 654 nm, and it did not affect NIR-II emission at 1550 nm. When cypate encountered ·OH, the structure was destroyed, resulting in increased luminescence at 654 nm. Based on this, a proportional luminescent probe (I_{654}/I_{1150}) responding to ·OH was designed. The detection limit was 4.20 μM. In addition, the $NaErF_4$@$NaLuF_4$ nanoprobe was successfully used, in mice, for the diagnosis of arthritis in vivo. Similarly, different types of ratiometric ROS sensors have been constructed through different LnNCs and surface modifications of ROS-responsive organic dyes [44,89,90]. Among them, Liu et al. [44] used 1530 nm as the excitation light source to design an H_2O_2 sensor using up-conversion (I_{980}/I_{1180}), and Liao et al. [89,90] constructed the ROS sensor with dual excitation light sources ($I_{980\ Ex}/I_{808\ Ex}$). For the LnNCs NIR-II sensing of ROS, organic dyes are mainly used as response units, and the sensing is realized by affecting the NIR-II luminescence through organic dyes.

4.1.2. HClO

HClO is a weakly acidic reactive oxygen species, which has the physiological defense functions of antibacterial and anti-inflammatory. However, with the increase in HClO concentration, tissue damage and some diseases may occur, such as neuronal degeneration, arthritis, and so on [91–95].

Wang et al. [91] constructed a proportional luminescent probe, based on the Er^{3+} emission of 1550 nm, to detect the inflammatory site HOCl in vivo (Figure 8a). Here, the Cy7.5 fluorophore was chosen as the HOCl-responsive molecule. The Cy7.5 influenced the luminescence at 1550 nm through the selective absorption of different excitation light sources ($I_{980\ Ex}/I_{808\ Ex}$). Under 808 nm excitation, Cy7.5 had a stronger absorption at 808 nm, which greatly weakened the absorption of 808 nm by probe, resulting in weaker

luminescence of Er^{3+} at 1530 nm. When HOCl molecules existed, Cy7.5 was degraded to weaken its absorption of 808 nm excitation. On the contrary, it enhanced the intensity of Er^{3+} NIR-II emission. Under 980 nm excitation, the luminescent intensity of Er^{3+} in 1550 nm remained almost unchanged, due to the weak absorption of Cy7.5 at 980 nm (Figure 8b). Therefore, under dual excitation wavelength irradiation, the ratio of the 1550 nm luminescent intensity of the two was closely related to the concentration of HOCl. The HOCl detection limit of the probe was 500 nmol/L, the resolution was 477 μm, and the detection depth was 3.5 mm in the living lymphoid inflammation model. Similarly, Zhang et al. [92] also designed a highly reactive oxygen species (HROS) sensor using dual excitation light sources ($I_{980\ Ex}/I_{808\ Ex}$). The detection limits for HOCl and ·OH were calculated as 0.3 and 1.6 μM, respectively. However, Cao et al. [93] reported a NIR-II ratio luminescent probe ($I_{925\ nm}/I_{1525\ nm}$) with a single excitation light source ($I_{808\ Ex}$) to detect HOCl by attaching organic dye Cy925 to the surface of $NaYbF_4$: Er@$NaYF_4$: Yb@$NaYF_4$: Nd (Figure 8c). The response unit of HOCl is Cy925, which, itself, emits light at 925 nm. When Cy925 encounters HOCl, the structure of Cy925 will be destroyed, resulting in weakening of the fluorescence at 925 nm. The luminescence of Er^{3+}, itself, at 1525 nm is not affected by HOCl. The detection range of the ratio probe for HOCl was 1~24 μM. The sensing of LnNCs NIR-II in HClO is similar to ROS, which is mainly realized by different organic dyes responding to HClO.

4.1.3. Glutathione (GSH)

GSH is an important endogenous antioxidant in the human body, which plays a vital role in the process of cell defense against toxins and free radical production. GSH has also been proven to be an important serum biochemical marker for the diagnosis of many diseases [96,97].

Wang et al. [96] reported a NIR-II nanoprobe consisting of 4-nitrophenol-Cy7 (NPh) conjugated LnNCs ($NaYF_4$: 20%Yb, 2%Er@$NaYF_4$: 30%Nd) for in vivo ratiometric sensing of GSH (Figure 8d). The GSH-responsive dye, NPh, has a strong absorption peak at 786 nm. Meanwhile, NPh has no fluorescence due to the presence of intramolecular photoinduced electron transfer (PET). In the presence of GSH, NPh reacted with GSH to generate Cy7-SG, the PET disappeared, and fluorescence recovered. Under 808 nm, Cy7-SG absorbed the energy of 808 nm, and transferred the excitation energy to LnNCs through energy transfer process, thereby achieving sensitization to LnNCs and enhanced luminescence at 1550 nm (Figure 8e). In addition, the 980 nm laser could not excite Cy7-SG, the luminescence at 1550 nm remained unchanged (Figure 8f), resulting in a ratio luminescence signal ($I_{808\ Ex}/I_{980\ Ex}$). The ratiometric $I_{808\ Ex}/I_{980\ Ex}$ value exhibited a linear ship with GSH concentration, ranging from 0~24 mM, with a detection limit of 0.3 mM. This dual excitation light source can effectively realize the sensing of GSH. However, the different absorption of different excitation light sources in vivo may lead to different detection depths and limits in different tissues.

4.1.4. $ONOO^-$

$ONOO^-$ is a very strong oxidant and plays an important role as an inflammatory mediator in physiology and pathology. $ONOO^-$ and its secondary reactants can oxidize and destroy various biological molecules, such as proteins, lipids, and nucleic acids. This process has been implicated in cardiovascular disease, neurodegenerative diseases, host defense, and antitumor immune responses [51,98,99,104].

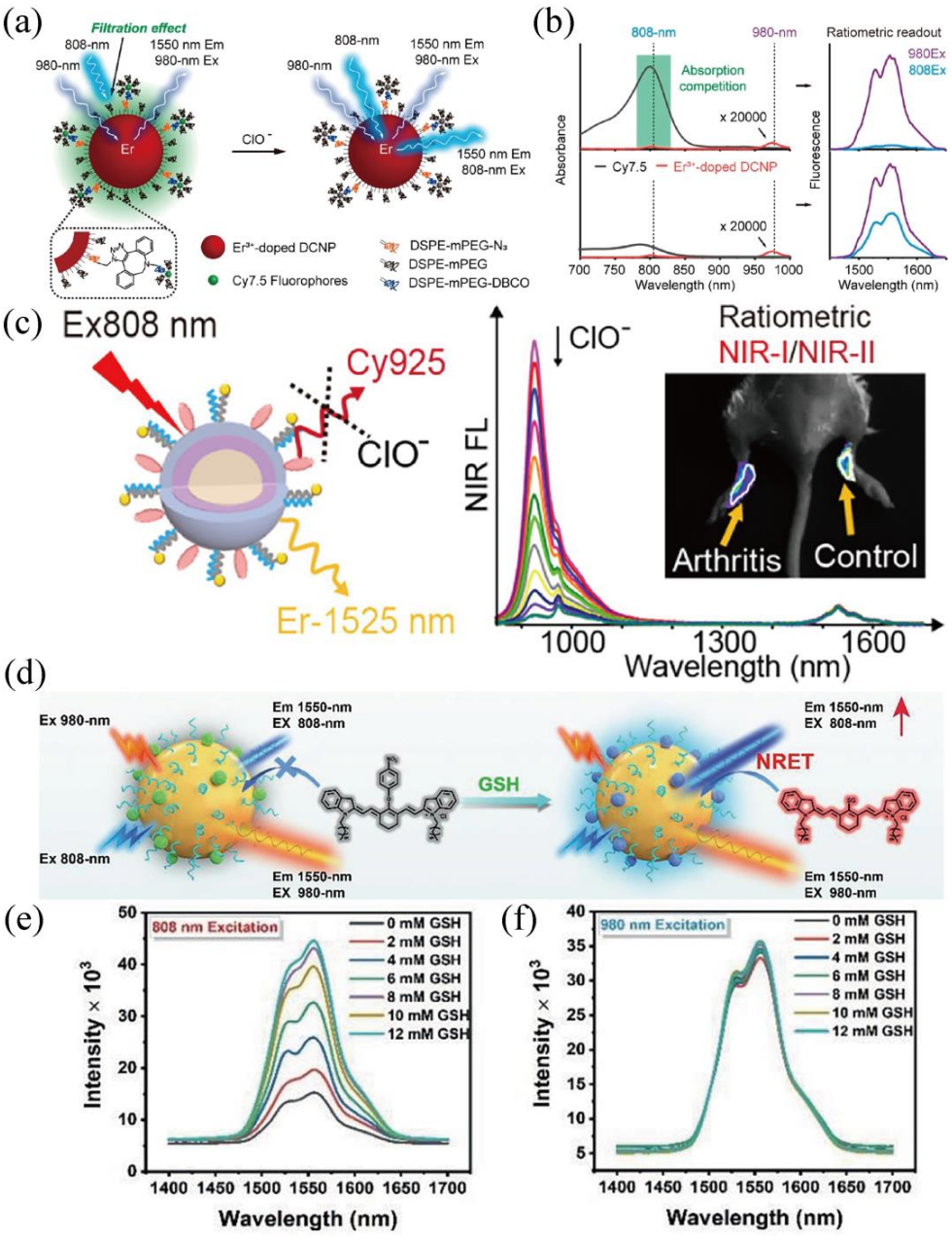

Figure 8. (**a**,**b**) Schematic design of the LnNCs@Cy7.5 for ClO^- detection. Adapted, with permission, from Ref. [91]. Copyright 2019, American Chemical Society. (**c**) Schematic illustration of the LnNCs@Cy925 for ClO^- detection. Adapted, with permission, from Ref. [93]. Copyright 2019, American Chemical Society. (**d**) Schematic illustration of the LnNCs@NPh for GSH detection. (**e**,**f**) NIR−II spectra of the LnNCs@NPh under 808 nm and 980 nm, respectively. Adapted, with permission, from Ref. [96]. Copyright 2021, Wiley−VCH.

Zhao et al. [98] designed and synthesized the $ONOO^-$ response $NaYF_4$@$NaYF_4$: 1%Nd^{3+}@MY-1057 probe (Figure 9a). $NaYF_4$@$NaYF_4$: 1%Nd^{3+} absorbed 808 nm excitation energy and produced NIR-II luminescence at 1060 nm. MY-1057 molecules existed as response units that respond to $ONOO^-$ and had a strong absorption at 1060 nm, thereby reducing the luminescent lifetime and intensity at 1060 nm. When $ONOO^-$ existed, MY-1057 dye was degraded and the luminescent lifetime and intensity were restored (Figure 9b,c). The probe had no reference signal and was especially affected by tissue depth when using luminescent intensity for $ONOO^-$ quantification. The slopes of intensity of the $ONOO^-$ functions were 900, 432, and 60 a.u. μm^{-1} under 0, 2, and 5 mm penetration depth, re-

spectively (Figure 9d). This illustrates the unreliable quantitative detection of $ONOO^-$ using intensity imaging based on signal attenuation due to homogeneous scattering and absorption. In contrast, consistent lifetime response was obtained regardless of penetration depth. Under phantom tissue with various penetration depths, lifetime values exhibited linear correspondence to $ONOO^-$ concentration, and the lifetime $ONOO^-$ function slopes were almost identical (Figure 9e). When no reference signal was present, the luminescent lifetime was taken as the signal with better stability and penetration depth than the luminescent intensity as the signal. Therefore, using the luminescence lifetime of LnNCs NIR-II as a signal to realize sensing may be a better research direction.

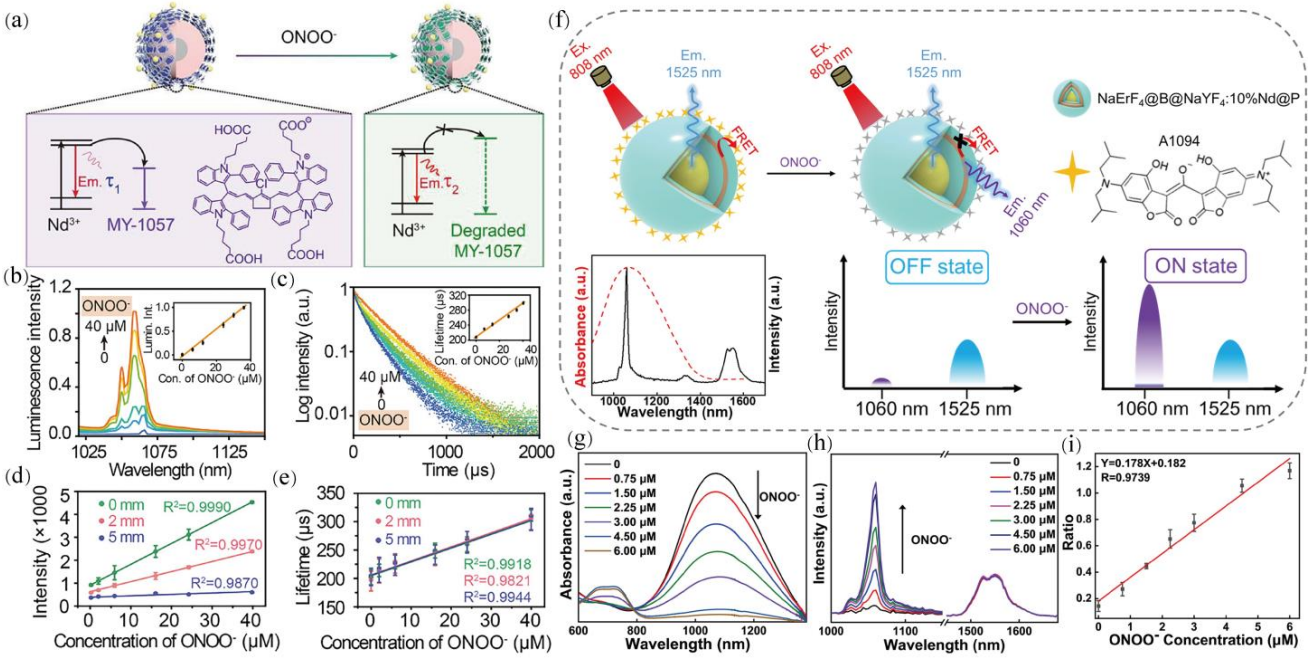

Figure 9. (**a**) Schematic design of the LnNCs@MY−1057 for $ONOO^-$ detection. (**b**) Luminescence emission intensity of LnNCs@MY−1057. (**c**) Lifetime response of LnNCs@MY-1057. (**d**) Plot of intensity changes under different penetration depths. (**e**) Plot of lifetime changes under different penetration depths. Adapted, with permission, from Ref. [98]. Copyright 2020, Wiley−VCH. (**f**) Schematic design of the LnNCs@A1094 for $ONOO^-$ detection. (**g**) Absorption spectra and (**h**) NIR−II spectra of LnNCs@A1094 upon gradual addition of $ONOO^-$. (**i**) Plot of fluorescence ratio (I_{1060}/I_{1525}) changes as a function of $ONOO^-$ concentration. Adapted, with permission, from Ref. [51]. Copyright 2021, American Chemical Society.

Sun et al. [51] tactfully designed a ratio type NIR-II probe (Figure 9f) that was constructed by modifying organic dyes A1094, responsive to $ONOO^-$, on the surface of LnNCs ($NaErF_4$@$NaYF_4$@$NaYF_4$: 10%Nd@$NaYF_4$). The LnNCs exhibited two NIR-II luminescence emissions of 1525 nm from Er^{3+} and 1060 nm from Nd^{3+}. Due to the substantial overlap between the A1094 absorbance at 1094 nm and the LnNCs@A1094 emission at 1060 nm, the 1060 nm emission was quenched by A1094 via the efficient Förster resonance energy transfer. The $ONOO^-$ is a highly specific oxidant of A1094, which can destroy its absorbance at 1094 nm. Therefore, the emission at 1060 nm of LnNCs@A1094 could be activated in the presence of $ONOO^-$ (Figure 9g). Meanwhile, A1094 had no effect on the luminescence at 1525 nm of LnNCs@A1094 (Figure 9h). The ratiometric luminescent intensity (I_{1060}/I_{1525}) of LnNCs@A1094 increased, linearly, with the augment of $ONOO^-$ concentration in the range of 0~6 μM, and the detection limit was 0.8 μM (Figure 9i).

4.1.5. H_2S

H_2S is the third gas signal molecule discovered after NO and CO. It plays an important role in the pathogenesis of neurodegenerative diseases, diabetes, heart failure, inflammation, cancer, and other diseases [87,100,101].

Liu et al. [100] developed a NIR-II luminescent LnNCs ($NaGdF_4$:2%Nd@$NaGdF_4$) probe for sensitive and selective sensing of H_2S. In this probe, the H_2S response unit is compound 1, which has high absorption at 808 nm (Figure 10a). Due to the weakening of the luminescent intensity of 808 nm excitation, the NIR-II emission at 1060 nm (Nd^{3+}) was weakened (Figure 10b). After the reaction with H_2S, the nucleophilic addition reaction between H_2S and the benzpyrole group in compound 1 could bleach the absorption of compound 1 at 808 nm and recover the 1060 nm emission of LnNCs (Figure 10c). The luminescent intensity at 1060 nm exhibited a good linear relationship in the range from 5 to 750 μM, and the detection limit was 17 nM.

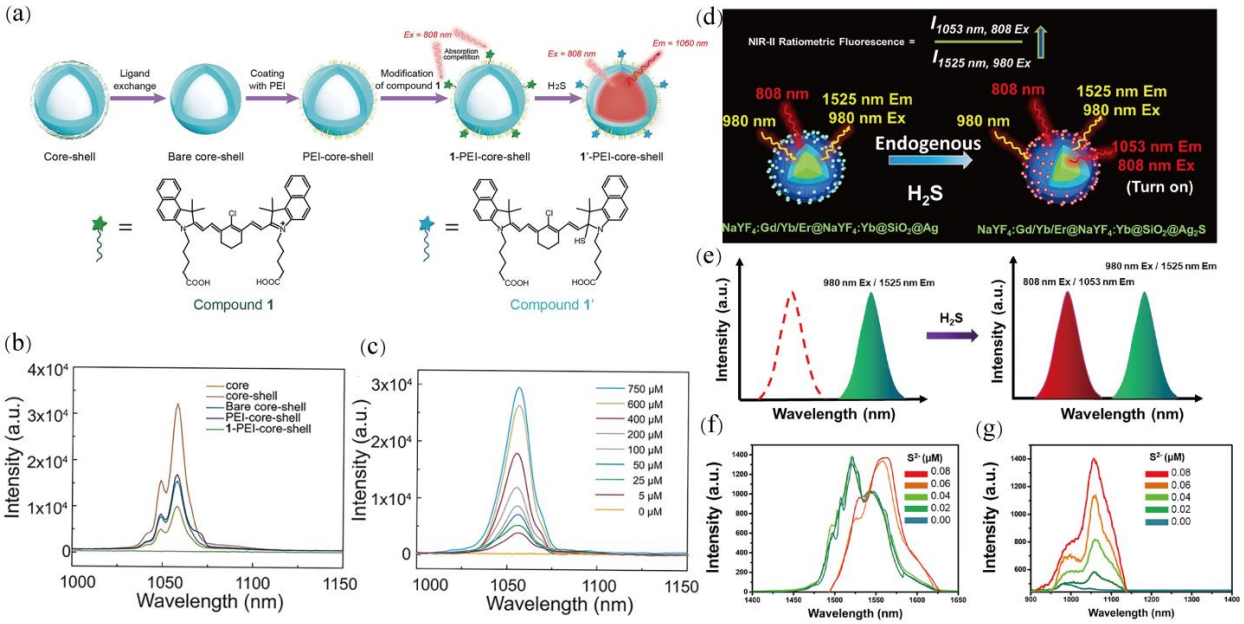

Figure 10. (**a**) Schematic illustration for the synthesis route of 1−PEI−LnNCs. (**b**) NIR−II luminescence spectra of 1−PEI−LnNCs. (**c**) NIR-II spectra of 1-PEI-LnNCs upon gradual addition of Na_2S. Adapted, with permission, from Ref. [100]. Copyright 2021, American Chemical Society. (**d**) Rational design of activatable orthogonal NIR−II emitting LnNCs@SiO_2@Ag nanoprobes for H_2S. (**e**) Activatable ratiometric fluorescence probe with H_2S responsive turn-on orthogonal NIR−II emission. (**f**,**g**) NIR−II spectra by adding different concentrations of Na_2S under 980 nm and 808 nm, respectively. Adapted, with permission, from Ref. [101]. Copyright 2021, American Chemical Society.

Compared with NIR-II probes that use organic dyes to achieve H_2S response, Deng et al. [101] achieved H_2S responsive NIR-II ratio probes by coating LnNCs ($NaYF_4$: Gd, Yb, Er@$NaYF_4$: Yb) with SiO_2 and Ag nanodots (Figure 10d). Here, Ag nanodots were used as the signal unit of H_2S response. After sulfidation with S^{2-}, LnNCs@SiO_2@Ag was quickly converted to LnNCs@SiO_2@Ag_2S. Under 980 nm laser, the luminescence of LnNCs@SiO_2@Ag and LnNCs@SiO_2@Ag_2S at 1525 nm were basically unchanged. It did not change with the increase in the amount of H_2S, which could be used as a reference signal (Figure 10e,f). Under 808 nm excitation, LnNCs@SiO_2@Ag has no luminescence emission at 1053 nm. However, when Ag_2S was formed, LnNCs@SiO_2@Ag_2S had a significant luminescence emission at 1053 nm under excitation at 808 nm (Figure 10e,g). Using the detection ($I_{808\ Ex/1053\ Em}$) and reference ($I_{980\ Ex/1525\ Em}$) signals, the NIR-II ratiometric luminescence signal, presented linearly, increases via improving the content of Na_2S from 0 to 0.08 μM, and the detection limit was 0.7 nM. More importantly, the in situ highly specific

ratiometric imaging of the metformin-induced hepatotoxicity was successfully achieved by using the activatable orthogonal NIR-II emitting probe. Compared with organic dyes as the response unit, Ag, as the response unit, has better responsiveness and detection limit for H_2S. The main reason for this may be that the Ag has better stability and is less prone to falling off.

4.2. Chemical Species

In vivo tracking of drug carriers and monitoring of drug release processes are of great significance for evaluating drug delivery efficiency and pharmacokinetics. Wang et al. [102] proposed a competitive absorption strategy based on the multi-wavelength excitation characteristics of LnNCs ($NaGdF_4$: 5%Nd@$NaGdF_4$), and designed a micron-sized oral drug carrier that could monitor the release process of protein drugs in the intestine (Figure 11a). They coated LnNCs in a shell of silica. Then, its surface was wrapped a layer of mesoporous silica to form SiO_2-Nd@SiO_2@mSiO_2-NH_2 (mSiO_2-Nd) (Figure 11b). Protein drugs (BSA) and tetrasulfonated phthalocyanine sodium salt (NPTAT) will form BSA-NPTAT complexes due to electrostatic interactions. The high absorption coefficient of the NPTAT, at 730 nm, could dramatically quench the 1060 nm luminescence of mSiO_2-Nd when excited by 730 nm (Figure 11c,d). While under 808 nm excitation, the mSiO_2-Nd 1060 nm emission was barely influenced by the NPTAT due to the weak absorbance of NPTAT at 808 nm. When BSA-NPTAT was loaded into mSiO_2-Nd, the release process of the drug was monitored and quantified by the emission at 1060 nm under the dual excitation light source (I_{730}/I_{808}). With the gradual release of BSA-NPTAT, the luminescence of Nd^{3+}, under excitation at 730 nm, also gradually recovered. The ratio of I_{730}/I_{808} reflected the degree of drug release (Figure 11e).

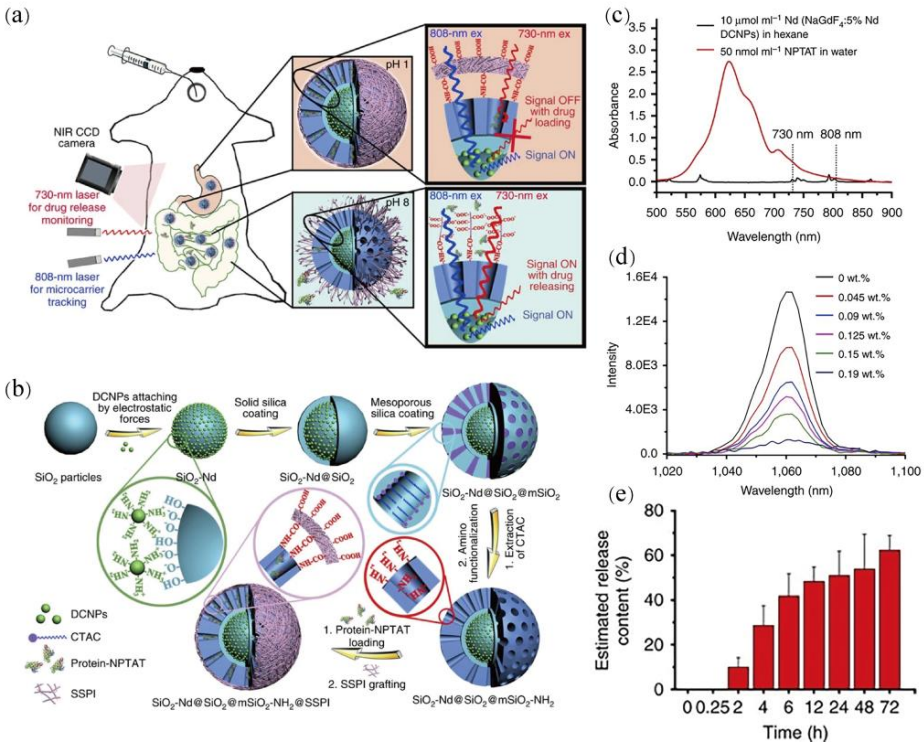

Figure 11. (**a**) Schematic of in vivo mSiO_2−Nd tracking and drug release monitoring by NIR−II emission. (**b**) Experimental processes of designing the NIR−II mesoporous microcarriers. (**c**) Absorption spectra of LnNCs dispersed in hexane and NPTAT dispersed in water. (**d**) NIR−II signals, as a function of the NPTAT loading amounts in the microcarrier, under 730 nm excitation. (**e**) In vivo release percentages of BSA−NPTAT. Adapted, with permission, from Ref. [102]. Copyright 2017, Springer Nature.

The LnNCs NIR-II luminescence applications in chemical sensing are seldom compared to the broad applications in biosensing. The main reason is that the biggest bright spot of the current NIR-II luminescence, compared with the luminescence of other regions, is the deeper tissue penetration and lower biological background interference. Meanwhile, NIR-II luminescence requires a specific and expensive NIR-II luminous receiver. Therefore, the application of NIR-II chemical sensing can only be based on the distribution of pharmaceutical chemicals or the concentration of chemical substances in organisms. Recently, Su et al. [103] developed an LnNCs NIR-II probe to detect inorganic pyrophosphate (PPi) in vivo for the first time. However, there are very few reports on the NIR-II sensing of LnNCs for chemical substances in vivo, which is also a direction for future sensing research.

5. Conclusions and Outlook

In this paper, NIR-II luminescent LnNCs-based bio/chemo sensors are reviewed. Firstly, the luminescence mechanism of LnNCs is briefly presented, followed by the enhancement strategies of their NIR-II luminescence (ion doping, core-shell structure, and dye sensitization) and preparing methods (thermal decomposition, hydrothermal synthesis, and co-deposition method). We then comprehensively review the sensing mechanism of the LnNCs-based bio/chemo sensors, as well as their applications in detection of various chemical and biomedical-related species. Obviously, NIR-II LnNCs-based bio/chemo sensors show a great prospect in biomedical sensing and imaging. However, they also confront some practical problems when working under physiological environments.

One is the luminescence quenching of NIR-II LnNCs by ambient hydroxyl groups in aqueous medium [2,37]. Although core-shell structure has been proved to be an effective strategy to isolate Ln^{3+} ions from external environment, the non-radiative decay by hydroxyl group is very efficient. This put forwards strict requirements for shell coating, which should not only be thick enough to shield the vibrational decaying of nearby hydroxyl groups but should also be compact enough to prevent the infiltrating of H_2O molecules. On the other hand, the quantum yield of LnNCs is not high (<30%) due to its structure and lattice defects [12,36]. Higher luminescence can be achieved by structural design, doping ions to fill emission levels, or building shell structures in nanoparticles, but this also creates high requirements for synthesis conditions, which is not conducive to large-scale production and subsequent applications. The LnNCs-based bio/chemo sensors show rather weak luminescent intensity because of the inherent small absorption cross-section of Ln^{3+} ions.

In addition, organic dyes are commonly used as fluorescent probes in LnNCs-based bio/chemo sensors [36]. The coupling between organic dyes and organic LnNCs needs to be considered in case of dye leakage, which may reduce the sensing accuracy. It is well known that most of these emissions lie in the visible range, which would degrade the performance of NIR-II sensors with shallow penetration depth. Hence, it is urgent to develop more fluorescent organic probes with NIR emission to match the strong penetrability of NIR-II LnNCs. Meanwhile, current research shows that most LnNPs are harmless luminescent probes suitable for living cells and mice [38,39,105]. However, the application of LnNPs in the body system is still limited due to the complex environment and metabolic processes in the body. There is an urgent need for a systematic and comprehensive assessment of their toxicity and stability in cells and animals.

Last but not least, NIR-II luminescent LnNCs-based bio/chemo sensors exhibit high sensitivity by virtue of deep penetration and background-free detection, but this is at the cost of expensive detectors, such as InGaAs [41,42,105]. This severely hampers their widespread applications in the biomedical realm, particularly in the case of lifetime-based detection. NIR-II LnNCs-based bio/chemo sensors may witness broader applications with the further development of NIR photodetectors.

Author Contributions: Conceptualization, T.Y., J.Q. and H.P.; methodology, T.Y., J.Q. and J.Z.; software, J.Z. and L.G.; validation, T.Y., J.Z. and L.G.; formal analysis, X.W. and M.Y. (Mei You); investigation, J.Z., M.Y. (Mu Yang) and L.G.; resources, H.P.; data curation, T.Y., J.Q. and H.P.; writing—original draft preparation, T.Y.; writing—review and editing, T.Y., J.Q. and H.P.; visualization, T.Y., L.G. and

H.P.; supervision, M.Y. (Mu Yang) and H.P.; project administration, H.P.; funding acquisition, H.P. All authors have read and agreed to the published version of the manuscript.

Funding: This work by the National Natural Science Foundation of China (Grant Nos.62175266, 61775245) and the Interdisciplinary Research Project of MUC (2020MDJC10).

Institutional Review Board Statement: Not applicable.

Informed Consent Statement: Not applicable.

Data Availability Statement: Not applicable.

Acknowledgments: We gratefully acknowledge support of this work by the National Natural Science Foundation of China (Grant Nos.62175266, 61775245) and the Interdisciplinary Research Project of MUC (2020MDJC10).

Conflicts of Interest: The authors declare no conflict of interest.

References

1. Liu, Y.; Li, Y.; Koo, S.; Sun, Y.; Liu, Y.; Liu, X.; Pan, Y.; Zhang, Z.; Du, M.; Lu, S.; et al. Versatile types of inorganic/organic NIR-IIa/IIb fluorophores: From strategic design toward molecular imaging and theranostics. *Chem. Rev.* **2022**, *122*, 209–268. [CrossRef] [PubMed]
2. Zhang, S.T.; Wang, Y.H.; Zhang, H.J. Lanthanide-doped fluorescence probes for NIR-II fluorescence imaging. *Chin. J. Lumin.* **2020**, *41*, 1460–1478. [CrossRef]
3. Bhat, M.P.; Kurkuri, M.; Losic, D.; Kigga, M.; Altalhi, T. New optofluidic based lab-on-a-chip device for the real-time fluoride analysis. *Anal. Chim. Acta* **2021**, *1159*, 338439. [CrossRef] [PubMed]
4. Purves, R.W.; Souster, K.; West, M.; Huda, A.M.; Fisher, C.M.E.; Belford, M.W.; Shurmer, B.O. Improved thyreostatic drug detection in animal tissues using liquid chromatography-high-field asymmetric waveform ion mobility spectrometry-mass spectrometry. *J. Agric. Food Chem.* **2022**, *70*, 4785–4791. [CrossRef] [PubMed]
5. Wang, J. Electrochemical detection for microscale analytical systems: A review. *Talanta* **2002**, *56*, 223–231. [CrossRef]
6. An, X.; Zhu, X.; Liu, J.; Zou, L.; Li, G.; Ye, B. Ratiometric fluorescence detection of ciprofloxacin using the terbium-based coordination polymers. *Spectrochim. Acta A* **2022**, *269*, 120775. [CrossRef]
7. Liu, S.; Yan, L.; Huang, J.; Zhang, J.; Zhou, B. Controlling upconversion in emerging multilayer core-shell nanostructures: From fundamentals to frontier applications. *Chem. Soc. Rev.* **2022**, *51*, 1729–1765. [CrossRef]
8. Cai, L.; Wang, Z.; Lin, B.; Liu, K.; Wang, Y.; Yuan, Y.; Tao, X.; Lv, R. Rare earth nanoparticles for sprayed and intravenous NIR II imaging and photodynamic therapy of tongue cancer. *Nanoscale Adv.* **2022**, *4*, 2224–2232. [CrossRef]
9. Tao, W.; Farokhzad, O.C. Theranostic nanomedicine in the NIR-II window: Classification, fabrication, and biomedical applications. *Chem. Rev.* **2022**, *122*, 5405–5407. [CrossRef]
10. Liang, T.; Guo, Z.; He, Y.; Wang, Y.; Li, C.; Li, Z.; Liu, Z. Cyanine-doped lanthanide metal-organic frameworks for near-Infrared II bioimaging. *Adv. Sci.* **2022**, *9*, 2104561. [CrossRef]
11. Zhao, M.Y.; Li, B.H.; Zhang, H.X.; Zhang, F. Activatable fluorescence sensors for in vivo bio-detection in the second near-infrared window. *Chem. Sci.* **2021**, *12*, 3448. [CrossRef] [PubMed]
12. Ge, X.Q.; Wei, R.Y.; Sun, L.N. Lanthanide nanoparticles with efficient near-infrared-II emission for biological applications. *J. Mater. Chem. B* **2020**, *8*, 10257. [CrossRef] [PubMed]
13. Diao, S.; Hong, G.S.; Antaris, A.L.; Blackburn, J.L.; Cheng, K.; Cheng, Z.; Dai, H.J. Biological imaging without autofluorescence in the second near-infrared region. *Nano Res.* **2015**, *8*, 3027–3034. [CrossRef]
14. Hong, G.S.; Antaris, A.L.; Dai, H.J. Near-infrared fluorophores for biomedical imaging. *Nat. Biomed. Eng.* **2017**, *1*, 0010. [CrossRef]
15. Naczynski, D.J.; Tan, M.C.; Zevon, M.; Wall, B.; Kohl, J.; Kulesa, A.; Chen, S.; Roth, C.M.; Riman, R.E.; Moghe, P.V. Rare-earth-doped biological composites as in vivo shortwave infrared reporters. *Nat. Commun.* **2013**, *4*, 2199. [CrossRef]
16. Tsukasaki, Y.; Komatsuzaki, A.; Mori, Y.; Ma, Q.; Yoshioka, Y.; Jin, T. A short-wavelength infrared emitting multimodal probe for non-invasive visualization of phagocyte cell migration in living mice. *Chem. Commun.* **2014**, *50*, 14356–14359. [CrossRef]
17. Lei, Z.H.; Zhang, F. Molecular engineering of NIR-II fluorophores for improved biomedical detection. *Angew. Chem. Int. Ed.* **2021**, *133*, 16430–16444. [CrossRef]
18. Zhong, Y.; Dai, H.J. A mini-review on rare-earth down-conversion nanoparticles for NIR-II imaging of biological systems. *Nano Res.* **2020**, *13*, 1281–1294. [CrossRef]
19. Tang, Y.F.; Pei, F.; Lu, X.M.; Fan, Q.L.; Huang, W. Recent advances on activatable NIR-II fluorescence probes for biomedical imaging. *Adv. Opt. Mater.* **2019**, *7*, 1900917. [CrossRef]
20. Kong, Y.; Chen, J.; Fang, H.; Heath, G.; Wo, Y.; Wang, W.; Li, Y.; Guo, Y.; Evans, S.D.; Chen, S.; et al. Highly fluorescent ribonuclease-A-encapsulated lead sulfide quantum dots for ultrasensitive fluorescence in vivo imaging in the second near-infrared window. *Chem. Mater.* **2016**, *28*, 3041–3050. [CrossRef]

21. Yang, T.; Tang, Y.; Ling Liu, L.; Lv, X.Y.; Wang, Q.L.; Ke, H.; Deng, Y.B.; Yang, H.; Yang, X.; Liu, G.; et al. Size-dependent Ag_2S nanodots for second near-infrared fluorescence/photoacoustics imaging and simultaneous photothermal therapy. *ACS Nano* **2017**, *11*, 1848–1857. [CrossRef] [PubMed]
22. Robinson, J.T.; Hong, G.; Liang, Y.; Zhang, B.; Yaghi, O.K.; Dai, H.J. In vivo fluorescence imaging in the second near-infrared window with long circulating carbon nanotubes capable of ultrahigh tumor uptake. *J. Am. Chem. Soc.* **2012**, *134*, 10664–10669. [CrossRef] [PubMed]
23. Wan, H.; Yue, J.; Zhu, S.; Uno, T.; Zhang, X.; Yang, Q.; Yu, K.; Hong, G.; Wang, J.; Li, L.; et al. A bright organic NIR-II nanofluorophore for three-dimensional imaging into biological tissues. *Nat. Commun.* **2018**, *9*, 1171. [CrossRef] [PubMed]
24. Dang, H.P.; Yan, L.F. Organic fluorescent nanoparticles with NIR-II emission for bioimaging and therapy. *Biomed. Mater.* **2021**, *16*, 022001. [CrossRef]
25. Wang, S.F.; Li, B.H.; Zhang, F. Molecular fluorophores for deep-tissue bioimaging. *ACS Cent. Sci.* **2020**, *6*, 1302–1316. [CrossRef]
26. Sun, W.; Guo, S.; Hu, C.; Fan, J.; Peng, X. Recent Development of chemosensors based on cyanine platforms. *Chem. Rev.* **2016**, *116*, 7768–7817. [CrossRef]
27. Wanderi, K.; Cui, Z.Q. Organic fluorescent nanoprobes with NIR-IIb characteristics for deep learning. *Exploration* **2022**, *2*, 20210097. [CrossRef]
28. Zhou, H.J.; Ren, T.B. Recent progress of cyanine fluorophores for NIR-II sensing and imaging. *Chem. Asian J.* **2022**, *17*, e202200147. [CrossRef]
29. Zhang, X.; Li, S.; Ma, H.; Wang, H.; Zhang, R.; Zhang, X.D. Activatable NIR-II organic fluorescent probes for bioimaging. *Theranostics* **2022**, *12*, 3345–3371. [CrossRef]
30. Yu, Z.; He, Y.; Schomann, T.; Wu, K.; Hao, Y.; Suidgeest, E.; Zhang, H.; Eich, C.; Cruz, L.J. Achieving effective multimodal imaging with rare-earth ion-doped CaF_2 nanoparticles. *Pharmaceutics* **2022**, *14*, 840. [CrossRef]
31. Xu, H.; Yang, Y.; Lu, L.; Yang, Y.; Zhang, Z.; Zhao, C.X.; Zhang, F.; Fan, Y. Orthogonal multiplexed NIR-II imaging with excitation-selective lanthanide-based nanoparticles. *Anal. Chem.* **2022**, *94*, 3661–3668. [CrossRef] [PubMed]
32. Wang, Q.X.; Yang, Y.F.; Yang, X.F.; Pan, Y.; Sun, L.D.; Zhang, W.Y.; Shao, Y.; Shen, J.; Lin, J.; Li, L.; et al. Upconverted/downshifted $NaLnF_4$ and metal-organic framework heterostructures boosting NIR-II imaging-guided photodynamic immunotherapy toward tumors. *Nano Today* **2022**, *43*, 101439. [CrossRef]
33. Lv, Z.; Jin, L.; Cao, Y.; Zhang, H.; Xue, D.; Yin, N.; Zhang, T.; Wang, Y.; Liu, J.; Liu, X.; et al. A nanotheranostic agent based on Nd^{3+}-doped YVO_4 with blood-brain-barrier permeability for NIR-II fluorescence imaging/magnetic resonance imaging and boosted sonodynamic therapy of orthotopic glioma. *Light Sci Appl* **2022**, *11*, 116. [CrossRef] [PubMed]
34. Gu, Y.; Guo, Z.; Yuan, W.; Kong, M.; Liu, Y.; Liu, Y.T.; Gao, Y.; Feng, W.; Wang, F.; Zhou, J.; et al. High-sensitivity imaging of time-domain near-infrared light transducer. *Nat. Photonics* **2019**, *13*, 525–531. [CrossRef]
35. Ding, S.W.; Lu, L.F.; Fan, Y.; Zhang, F. Recent progress in NIR-II emitting lanthanide-based nanoparticles and their biological applications. *J. Rare Earths* **2020**, *38*, 451–463. [CrossRef]
36. Fan, Y.; Zhang, F. A new generation of NIR-II probes: Lanthanide-based nanocrystals for bioimaging and biosensing. *Adv. Opt. Mater.* **2019**, *7*, 1801417. [CrossRef]
37. Wang, Z.; Xing, B.G. Near-infrared multipurpose lanthanide-imaging nanoprobes. *Chem.-Asian J.* **2020**, *15*, 2076–2091. [CrossRef]
38. Xu, J.; Gulzar, A.; Yang, P.P.; Bi, H.; Yang, D.; Gai, S.; He, F.; Lin, J.; Xing, B.G.; Jin, D.Y. Recent advances in near-infrared emitting lanthanide-doped nanoconstructs: Mechanism, design and application for bioimaging. *Coord. Chem. Rev.* **2019**, *381*, 104–134. [CrossRef]
39. Yang, Y.J.; Tu, D.; Zhang, Y.; Zhang, P.; Chen, X.Y. Recent advances in design of lanthanide-containing NIR-II luminescent nanoprobes. *iScience* **2021**, *24*, 102062. [CrossRef]
40. Zhang, M.Z.; Zhai, X.Y.; Sun, M.Z.; Ma, T.F.; Huang, Y.K.; Huang, B.L.; Du, Y.P.; Yan, C.H. When rare earth meets carbon nanodots: Mechanisms, applications and outlook. *Chem. Soc. Rev.* **2020**, *49*, 9220–9248. [CrossRef]
41. Yu, S.H.; Tu, D.; Lian, W.; Xu, J.; Chen, X.Y. Lanthanide-doped near-infrared II luminescent nanoprobes for bioapplications. *Sci. China Mater.* **2019**, *62*, 1071–1086. [CrossRef]
42. Lia, Z.; Ding, X.; Cong, H.; Wang, S.; Yu, B.; Shen, Y. Recent advances on inorganic lanthanide-doped NIR-II fluorescence nanoprobes for bioapplication. *J. Lumin.* **2020**, *228*, 117627. [CrossRef]
43. Zhang, H.X.; Fan, Y.; Pei, P.; Sun, C.; Lu, L.; Zhang, F. Tm^{3+}-sensitized NIR-II fluorescent nanocrystals for in vivo information storage and decoding. *Angew. Chem. Int. Ed.* **2019**, *58*, 10153–10157. [CrossRef] [PubMed]
44. Liu, L.; Wang, S.F.; Zhao, B.Z.; Pei, P.; Fan, Y.; Li, X.M.; Zhang, F. Er^{3+} sensitized 1530 nm to 1180 nm second near-infrared window upconversion nanocrystals for in vivo biosensing. *Angew. Chem. Int. Ed.* **2018**, *57*, 7518–7522. [CrossRef]
45. Li, Y.B.; Zeng, S.J.; Hao, J.H. Non-invasive optical guided tumor metastasis/vessel imaging by using lanthanide nanoprobe with enhanced down-shifting emission beyond 1500 nm. *ACS Nano* **2019**, *13*, 248–259. [CrossRef]
46. Zhong, Y.; Ma, Z.; Zhu, S.; Yue, J.; Zhang, M.; Antaris, A.L.; Yuan, J.; Cui, R.; Wan, H.; Zhou, Y.; et al. Boosting the down-shifting luminescence of rare-earth nanocrystals for biological imaging beyond 1500 nm. *Nat. Commun.* **2017**, *8*, 737. [CrossRef]
47. Zhong, Y.; Ma, Z.; Wang, F.; Wang, X.; Yang, Y.; Liu, Y.; Zhao, X.; Li, J.; Du, H.; Zhang, M.; et al. In vivo molecular imaging for immunotherapy using ultra-bright near-infrared-IIb rare-earth nanoparticles. *Nat. Biotechnol.* **2019**, *37*, 1322–1331. [CrossRef]

48. Tan, M.; Rosal, B.; Zhang, Y.; Rodríguez, E.M.; Hu, J.; Zhou, Z.; Fan, R.; Ortgies, D.H.; Fernández, N.; Chaves-Coira, I.; et al. Rare-earth-doped fluoride nanoparticles with engineered long luminescence lifetime for time-gated in vivo optical imaging in the second biological window. *Nanoscale* **2018**, *10*, 17771–17780. [CrossRef]
49. Li, H.; Wang, X.; Li, X.L.; Zeng, S.J.; Chen, G.Y. Clearable shortwave-infrared-emitting $NaErF_4$ nanoparticles for noninvasive dynamic vascular imaging. *Chem. Mater.* **2020**, *32*, 3365–3375. [CrossRef]
50. Fischer, S.; Bronstein, N.D.; Swabeck, J.K.; Chan, E.M.; Alivisatos, A.P. Precise tuning of surface quenching for luminescence enhancement in core-shell lanthanide-doped nanocrystals. *Nano Lett.* **2016**, *16*, 7241–7247. [CrossRef]
51. Sun, Z.; Huang, H.; Zhang, R.; Yang, X.; Yang, H.; Li, C.; Zhang, Y.; Wang, Q.B. Activatable rare earth near-infrared-II fluorescence ratiometric nanoprobes. *Nano Lett.* **2021**, *21*, 6576–6583. [CrossRef] [PubMed]
52. Wang, R.; Li, X.M.; Zhou, L.; Zhang, F. Epitaxial seeded growth of rare-earth nanocrystals with efficient 800 nm near-infrared to 1525 nm short-wavelength infrared down conversion photoluminescence for in vivo bioimaging. *Angew. Chem. Int. Ed.* **2015**, *126*, 12282–12286. [CrossRef]
53. Wang, Q.; Liang, T.; Wu, J.; Li, Z.; Liu, Z.H. Dye-sensitized rare earth-doped nanoparticles with boosted NIR-IIb emission for dynamic imaging of vascular network-related disorders. *ACS Appl. Mater. Interfaces* **2021**, *13*, 29303–29312. [CrossRef]
54. Shao, W.; Chen, G.Y.; Kuzmin, A.; Kutscher, H.L.; Pliss, A.; Ohulchanskyy, T.Y.; Prasad, P.N. Tunable narrow band emissions from dye-sensitized core/shell/shell nanocrystals in the second near-infrared biological window. *J. Am. Chem. Soc.* **2016**, *138*, 16192–16195. [CrossRef] [PubMed]
55. Wang, D.; Wang, D.; Kuzmin, A.; Pliss, A.; Shao, W.; Xia, J.; Qu, J.; Prasad, P.N. ICG-sensitized $NaYF_4$:Er nanostructure for theranostics. *Adv. Optical Mater.* **2018**, *6*, 1701142. [CrossRef]
56. Ren, F.; Liu, H.; Zhang, H.; Jiang, Z.; Xia, B.; Genevois, C.; He, T.; Allix, M.; Sun, Q.; Li, Z.; et al. Engineering NIR-IIb fluorescence of Er-based lanthanide nanoparticles for through-skull targeted imaging and imaging-guided surgery of orthotopic glioma. *Nano Today* **2020**, *34*, 100905. [CrossRef]
57. Zhang, W.; Chen, T.; Su, L.; Ge, X.; Chen, X.Y.; Song, J.B.; Yang, H.H. Quantum dot-based sensitization system for boosted photon absorption and enhanced second near-infrared luminescence of lanthanide-doped nanoparticle. *Anal. Chem.* **2020**, *92*, 6094–6102. [CrossRef]
58. Wang, F.; Deng, R.R.; Liu, X.G. Preparation of core-shell $NaGdF_4$ nanoparticles doped with luminescent lanthanide ions to be used as upconversion-based probes. *Nat. Protoc.* **2014**, *9*, 1634–1644. [CrossRef]
59. Suter II, J.D.; Pekas, N.J.; Berry, M.T.; May, P.S. Real-time-monitoring of the synthesis of β-$NaYF_4$:17% Yb, 3% Er nanocrystals using NIR-to-visible upconversion luminescence. *J. Phys. Chem. C* **2014**, *118*, 13238–13247. [CrossRef]
60. Li, D.D.; Shao, Q.Y.; Dong, Y.; Jiang, J.Q. Phase-, shape- and size-controlled synthesis of $NaYF_4$:Yb^{3+},Er^{3+} nanoparticles using rare-earth acetate precursors. *J. Rare Earth.* **2014**, *32*, 1032–1036. [CrossRef]
61. Chen, B.; Kong, W.; Wang, N.; Zhu, G.Y.; Wang, F. Oleylamine-mediated synthesis of small $NaYbF_4$ nanoparticles with tunable size. *Chem. Mater.* **2019**, *31*, 4779–4786. [CrossRef]
62. Rastogi, C.K.; Lu, E.; Tam, J.; Pichaandi, J.M.; Howe, J.; Winnik, M.A. Influence of the sodium precursor on the cubic-to-hexagonal phase transformation and controlled preparation of uniform $NaNdF_4$ nanoparticles. *Langmuir* **2021**, *37*, 2146–2152. [CrossRef] [PubMed]
63. Huang, P.; Zheng, W.; Gong, Z.; You, W.; Wei, J.; Chen, X. Rare earth ion- and transition metal ion-doped inorganic luminescent nanocrystals: From fundamentals to biodetection. *Mater. Today Nano* **2019**, *5*, 100031. [CrossRef]
64. You, W.; Tu, D.; Zheng, W.; Shang, X.; Song, X.; Zhou, S.; Liu, Y.; Li, R.; Chen, X. Large-scale synthesis of uniform lanthanide-doped $NaREF_4$ upconversion/ downshifting nanoprobes for bioapplications. *Nanoscale* **2018**, *10*, 11477–11484. [CrossRef] [PubMed]
65. Cheng, X.; Ge, H.; Wei, Y.; Zhang, K.; Su, W.; Zhou, J.; Yin, L.; Zhan, Q.; Jing, S.; Huang, L. Design for brighter photon upconversion emissions via energy level overlap of lanthanide ions. *ACS Nano* **2018**, *12*, 10992–10999. [CrossRef] [PubMed]
66. Wang, Y.; Gai, S.; Niu, N.; He, F.; Yang, P.P. Synthesis of $NaYF_4$ microcrystals with different morphologies and enhanced up-conversion luminescence properties. *Phys. Chem. Chem. Phys.* **2013**, *15*, 16795. [CrossRef]
67. Wang, L.; Li, Y.D. Controlled synthesis and luminescence of lanthanide doped $NaYF_4$ nanocrystals. *Chem. Mater.* **2007**, *19*, 727–734. [CrossRef]
68. Sun, L.; Wei, R.; Feng, J.; Zhang, H.J. Tailored lanthanide-doped upconversion nanoparticles and their promising bioapplication prospects. *Coordin. Chem. Rev.* **2018**, *364*, 10–32. [CrossRef]
69. Qu, X.; Pan, G.; Yang, H.K.; Chen, Y.; Chung, J.W.; Moon, B.K.; Choi, B.C.; Jeong, J.H. Solvothermal synthesis and luminescence properties of $NaYF_4$:Ln^{3+} (Eu^{3+}, Tb^{3+}, Yb^{3+}/Er^{3+}) nano- and microstructures. *Opt. Mater.* **2012**, *34*, 1007–1012. [CrossRef]
70. Zhou, Z.; Zheng, W.; Kong, J.; Liu, Y.; Huang, P.; Zhou, S.; Chen, Z.; Shi, J.; Chen, X. Rechargeable and LED-activated $ZnGa_2O_4$: Cr^{3+} near-infrared persistent luminescence nanoprobes for background-free biodetection. *Nanoscale* **2017**, *9*, 6846–6853. [CrossRef]
71. Cao, T.M.D.; Le, T.T.G.; Nguyen, T.P.N.; Dau, T.A.N.; Nguyen, V.T.; Tran, T.T.V. Investigating the effect of Yb^{3+} and Er^{3+} concentration on red/green luminescent ratio in β-$NaYF_4$: Er, Yb nanocrystals using spectroscopic techniques. *J. Mol. Struct.* **2020**, *12*, 128014. [CrossRef]
72. Carniato, F.; Thangavel, K.; Tei, L.; Botta, M. Structure and dynamics of the hydration shells of citrate-coated GdF_3 nanoparticles. *J. Mater. Chem. B* **2013**, *1*, 2442. [CrossRef] [PubMed]
73. Evanics, F.; Diamente, P.R.; van Veggel, F.C.J.M.; Stanisz, G.J.; Prosser, R.S. Water-soluble GdF_3 and GdF_3/LaF_3 nanoparticless-physical characterization and NMR relaxation properties. *Chem. Mater.* **2006**, *18*, 2499. [CrossRef]

74. Bednarkiewicz, A.; Mech, A.; Karbowiak, M.; Strek, W. Spectral properties of Eu^{3+} doped $NaGdF_4$ nanocrystals. *J. Lumin.* **2005**, *114*, 247. [CrossRef]
75. Loo, J.F.C.; Chien, Y.H.; Yin, F.; Kong, S.K.; Ho, H.P.; Yong, K.T. Upconversion and downconversion nanoparticles for biophotonics and nanomedicine. *Coord. Chem. Rev.* **2019**, *400*, 213042. [CrossRef]
76. Donato, G.; Grosvenor, A.P. Crystallization of rare-earth phosphate-borosilicate glass composites synthesized by a one-step coprecipitation method. *Cryst. Growth Des.* **2020**, *20*, 2217–2231. [CrossRef]
77. Aleshin, D.K.; Mashkovtsev, M.A.; Kuznetsova, Y.A.; Rychkov, V.N.; Zatsepin, A.F.; Gordeev, E.V. Fabrication of $(Y_{0.95}Eu_{0.05})_2O_3$ phosphors with enhanced properties by coprecipitation of layered rare earth hydroxide. *J. Alloys Compd.* **2019**, *805*, 258–266. [CrossRef]
78. Yi, G.S.; Chow, G.M. Colloidal LaF_3: Yb, Er, LaF_3: Yb, Ho and LaF_3: Yb, Tm nanocrystals with multicolor upconversion fluorescence. *J. Mater. Chem.* **2005**, *15*, 4460–4464. [CrossRef]
79. Guan, H.; Feng, Y.; Zhang, W.; Wang, W.; Hu, Y. Room-temperature facile synthesis of hexagonal $NaYF_4$ and $NaYF_4$: Yb, Er powder without any organic additives and its upconversion fluorescence properties. *Adv. Powder Technol.* **2022**, *33*, 103381. [CrossRef]
80. Sarkar, D.; Meesaragandla, B.; Samanta, T.; Mahalingam, V. A greener approach towards making highly luminescent Ln^{3+}-doped $NaYF_4$ nanoparticles with ligand-assisted phase control. *ChemistrySelect* **2016**, *1*, 4785–4793. [CrossRef]
81. Wang, M.; Mi, C.C.; Wang, S.; Li, F.; Liu, J.L.; Xu, S.K. Synthesis and characterization of $NaYF_4$: Yb, Er upconversion fluorescent nanoparticles via a co-precipitation method. *Spectrosc. Spect. Anal.* **2009**, *29*, 3327–3331.
82. Sekiyama, S.; Umezawa, M.; Kuraoka1, S.; Ube, T.; Kamimura, M.; Soga, K. Temperature sensing of deep abdominal region in mice by using over-1000 nm near-infrared luminescence of rare-earth-doped $NaYF_4$ nanothermometer. *Sci. Rep.* **2018**, *8*, 16979. [CrossRef] [PubMed]
83. Kong, M.; Gu, Y.Y.; Chai, Y.; Ke, J.; Liu, Y.; Xu, X.; Li, Z.X.; Feng, W.; Li, F.Y. Luminescence interference-free lifetime nanothermometry pinpoints in vivo temperature. *Sci. China Chem.* **2021**, *64*, 974–984. [CrossRef]
84. Wang, Z.; Xu, H.; Jia, M.; Jin, X.; Lv, Z.; Dai, M.; Zhu, K.M.; Feng, J.; Ge, X.; Fu, Z. Multifunctional lanthanide ions-doped $Ba_2TiGe_2O_8$ phosphor for near-infrared ratiometric thermometer and information security. *J. Lumin.* **2022**, *243*, 118652. [CrossRef]
85. Nexha, A.; Carvajal, J.J.; Pujol, M.C.; Díaza, F.; Aguiló, M. Lanthanide doped luminescence nanothermometers in the biological windows: Strategies and applications. *Nanoscale* **2021**, *13*, 7913–7987. [CrossRef]
86. Lei, X.; Li, R.; Tu, D.; Shang, X.Y.; Liu, Y.; You, W.; Sun, C.; Zhang, F.; Chen, X.Y. Intense near-infrared-II luminescence from $NaCeF_4$: Er/Yb nanoprobes for in vitro bioas-say and in vivo bioimaging. *Chem. Sci.* **2018**, *9*, 4682–4688. [CrossRef]
87. Wang, C.; Niu, M.; Wang, W.; Su, L.; Feng, H.J.; Lin, H.X.; Ge, X.; Wu, R.; Li, Q.; Liu, J.; et al. In situ activatable ratiometric NIR-II fluorescence nanoprobe for quantitative detection of H_2S in colon cancer. *Anal. Chem.* **2021**, *93*, 9356–9363. [CrossRef]
88. Jia, Q.; Liu, Y.; Duan, Y.; Zhou, J. Interference-free detection of hydroxyl radical and arthritis diagnosis by rare earth-based nanoprobe utilizing SWIR emission as reference. *Anal. Chem.* **2019**, *91*, 11433–11439. [CrossRef]
89. Liao, N.; Su, L.; Zheng, Y.; Zhao, B.; Wu, M.; Zhang, D.; Yang, H.H.; Liu, X.L.; Song, J.B. In vivo tracking of cell viability for adoptive natural killer cell-based immunotherapy by ratiometric NIR-II fluorescence imaging. *Angew. Chem. Int. Ed.* **2021**, *133*, 2–11. [CrossRef]
90. Liao, N.; Su, L.; Cao, Y.; Qiu, L.; Xie, R.; Peng, F.; Cai, Z.; Liu, X.; Song, J.; Zeng, Y. Tracking cell viability for adipose-derived mesenchymal stem cell-based therapy by quantitative fluorescence imaging in the second near-infrared window. *ACS Nano* **2022**, *16*, 2889–2900. [CrossRef]
91. Wang, S.; Liu, L.; Fan, Y.; El-Toni, A.M.; Alhoshan, M.S.; Li, D.; Zhang, F. In vivo high-resolution ratiometric fluorescence imaging of inflammation using NIR-II nanoprobes with 1550 nm emission. *Nano Lett.* **2019**, *19*, 2418–2427. [CrossRef] [PubMed]
92. Zhang, M.; Wang, Z.; Wang, C.; Wu, Y.T.; Li, Z.; Liu, Z.H. Visualizing oxidative stress level for timely assessment of ischemic stroke via a ratiometric near-infrared-II luminescent nanoprobe. *ACS Nano* **2021**, *15*, 11940–11952. [CrossRef] [PubMed]
93. Cao, C.; Zhou, X.B.; Xue, M.; Han, C.; Feng, W.; Li, F.Y. Dual near-infrared-emissive luminescent nanoprobes for ratiometric luminescent monitoring of ClO^- in living organisms. *ACS Appl. Mater. Interfaces* **2019**, *11*, 15298–15305. [CrossRef]
94. Ge, X.; Lou, Y.; Su, L.; Chen, B.; Guo, Z.Y.; Gao, S.; Zhang, W.; Chen, T.; Song, J.B.; Yang, H.H. Single wavelength laser excitation ratiometric NIR-II fluorescent probe for molecule imaging in vivo. *Anal. Chem.* **2020**, *92*, 6111–6120. [CrossRef] [PubMed]
95. Pei, P.; Hu, H.; Chen, Y.; Wang, S.; Chen, J.; Ming, J.; Yang, Y.; Sun, C.; Zhao, S.; Zhang, F. NIR-II ratiometric lanthanide-dye hybrid nanoprobes doped bioscaffolds for in situ bone repair monitoring. *Nano Lett.* **2022**, *22*, 783–791. [CrossRef] [PubMed]
96. Wang, C.; Lin, H.; Ge, X.; Mu, J.; Su, L.; Zhang, X.; Niu, M.; Yang, H.H.; Song, J.B. Dye-sensitized downconversion nanoprobes with emission beyond 1500 nm for ratiometric visualization of cancer redox state. *Adv. Funct. Mater.* **2021**, *31*, 2009942. [CrossRef]
97. Li, Z.; Wu, J.; Wang, Q.; Liang, T.; Ge, J.; Wang, P.; Liu, Z. A universal strategy to construct lanthanide-doped nanoparticles-based activable NIR-II luminescence probe for bioimaging. *iScience* **2020**, *23*, 100962. [CrossRef]
98. Zhao, M.; Li, B.H.; Wu, Y.; He, H.; Zhu, X.; Zhang, H.; Dou, C.; Feng, L.; Fan, Y.; Zhang, F. A tumor-microenvironment-responsive lanthanide-cyanine FRET sensor for NIR-II luminescence-lifetime in situ imaging of hepatocellular carcinoma. *Adv. Mater.* **2020**, *32*, 2001172. [CrossRef]
99. Zhong, Y.; Gu, J.; Su, Y.; Zhao, L.; Zhou, Y.; Peng, J. Real-time screening of hepatotoxins in natural medicine by peroxynitrite responsive lanthanide-based NIR-II luminescent probes. *Chem. Eng. J.* **2022**, *433*, 133263. [CrossRef]

100. Liu, Q.; Zhong, Y.; Su, Y.; Zhao, L.Z.; Peng, J.J. Real-time imaging of hepatic inflammation using hydrogen sulfide-activatable second near-infrared luminescent nanoprobes. *Nano Lett.* **2021**, *21*, 4606–4614. [CrossRef]
101. Deng, Z.; Bi, S.; Jiang, M.Y.; Zeng, S.J. Endogenous H_2S-activated orthogonal second near-infrared emissive nanoprobe for in situ ratiometric fluorescence imaging of metformin-induced liver injury. *ACS Nano* **2021**, *15*, 3201–3211. [CrossRef] [PubMed]
102. Wang, R.; Zhou, L.; Wang, W.; Li, X.M.; Zhang, F. In vivo gastrointestinal drug-release monitoring through second near-infrared window fluorescent bioimaging with orally delivered microcarriers. *Nat. Commun.* **2017**, *8*, 14702. [CrossRef] [PubMed]
103. Su, Y.; Ye, L.; Gu, J.; Zhao, L.; Zhou, Y.; Peng, J. Sensing and imaging of PPi in vivo using lanthanide-based second near-infrared luminescent probes. *J. Mater. Chem. B* **2022**, *10*, 1055. [CrossRef] [PubMed]
104. Li, C.Y.; Li, W.F.; Liu, H.H.; Zhang, Y.J.; Chen, G.C.; Li, Z.J.; Wang, Q.B. An activatable NIR-II nanoprobe for in vivo early real-time diagnosis of traumatic brain injury. *Angew. Chem. Int. Ed.* **2020**, *59*, 247–252. [CrossRef]
105. Wu, Z.F.; Ke, J.X.; Liu, Y.S.; Sun, P.M.; Hong, M.C. Lanthanide-based NIR-II fluorescent nanoprobes and their biomedical applications. *Acta Chim. Sin.* **2022**, *80*, 542–552. [CrossRef]